High Performance Si AWG With Geometrically Improved Interface Between Slab And Waveguide Array

Simon Tristan Santacatterina

(Student ID No.: 81923479)

Advisor Professor: Tsuda Hiroyuki

September 2021

Keio University

Graduate School of Science and Technology

School of Integrated Design Engineering

Thesis Abstract

Arrayed Waveguide Gratings (AWG), also called PHASARS in the literature, are optical communication devices which play a key role in Wavelength Division Multiplexing (WDM), a technique considerably improving networks transmission capacity and flexibility. Taking light as an input and by the successive use of Fourier Optics transformation as well as a waveguide array, which provides the focusing and dispersive properties, the AWG are able to operate as wavelength multiplexers, demultiplexers and routers. This component has found a wide range of applications, for instance optical coupler/splitter, and is integrated with many other optical devices such as modulator, photodiode. Firstly built in silica which resulted in too bulky structures and with the advance of Si photonics technology, Si was therefore used for the miniaturization of AWGs. This has permitted to reach dimensions of one or two order of magnitude smaller. However, Si AWG's waveguides (WGs) enhanced optical confinement induces larger phase error and scattering/losses in transition regions. This is typically resulting in deteriorated performances of crosstalk and insertion loss. The most sensible region located at the abrupt transition, with a high index difference between *Si* and SiO_2, between the planar slab region and the arrayed WGs region, which yields to optical field mismatch in addition to scattering. This research is focused on improving this sensitive region by geometrically adapting the refractive index transition to reduce the loss and therefore increase the overlap integral in the waveguides. This is done by two main successive techniques. At first, a physically defined topology being optimized by the shape, length as well as choice of configuration, tested among several alternatives, for the transition tapers

and slab/waveguides etching. The field being generated by finite-difference time-domain (FDTD). And then, the introduction of etching in the FPR (free propagation region) for modification of the effective refractive index and decrease the impedance mismatch between two regions in which the light successively travels. The metric used for optimization is mainly the overlap integral although the normalized output power is sometime used. This overlap function being mathematically chosen to represent the coupling efficiency from the slabs to the WGs and inversely. The study demonstrate improvements compared to simple transition shapes usually used for those transition area and evaluate the device overall performances.

Chapter 1 introduces this work by describing the context around Si photonics and the objectives of this research.

Chapter 2 explains the theoretical background of AWGs and improvement techniques that are going to be used for our design.

Chapter 3 presents the theoretical background regarding the numerical methods used to solve for the fields and optimize the geometry.

Chapter 4 describes the simulations methods, set up and the results, then its present the AWG characteristics at each step of the device for the central wavelength with an efficient algorithm.

Chapter 5 concludes this work and summarizes the global point as well as exposes the limits and further possible improvements for the device.

Acknowledgments

First of all, I would like to start by thanking Keio University as a all and more particularly my professor Hiroyuki Tsuda for accepting me in his laboratory and allowing me to start a research on a completely new topic, while I had no previous knowledge in the field. Topic later found to be very interesting. Also, I would like to mention my lab mate Fumi Nakamura for the useful discussions I had with her. And finally all the other teachers who supported me during my international program such as Prof. Claude Oestges from the Polytechnic University of Louvain-La-Neuve. Thanks to them I was able to study interesting topics as well as acquire technical and applied knowledge in various fields of study. By giving me the opportunity to perform a double degree program I could deepen my interest in studies, while at the same time discover the Japanese culture and its specificity, meet a wide range of interesting people from different backgrounds and visit new places.

I also would like to thank my family. First and foremost, my mother and father that supported me throughout my entire university studies and research, years for which I had to provide a hard work. Also, for their support in my personal life and plans and my choice of coming in Japan for an experience abroad. All their support for the private nice environment they provided me cannot be accounted for. My brother as well for our long discussions, laughs and our close relationship. To that, I would like to add a particular thought for my grandmother Léonie.

In the end, a big thank to all the friends I have made in this new land of Japan. This stay will forever be engraved in my memory thanks to the memorable moments we had. Thanks

to Jocelyn for all the tips he brought me, to all the Shimodians of the first semester for our travels and the sensational moments and because we are still in touch and also to the Japanese friends I have made along the way.

Contents

viii

Chapter 1

Introduction

1.1 Context

Through the second part of the 20th centuries, the need for higher capacity networks led to an important breakthrough in communication technologies. Scientists started to introduce light as an efficient way of carrying information. Optical fibers were therefore introduced around 1970 as a new method, much more efficient than the previous copper wires, who reached their fundamental limitations, to transmit information in a compact and low-loss manner. Using low-loss fibers, the information can then be transmitted over longer distances and the transmission capacity increased, allowing transmission of a higher amount of data per unit of time (b/s). Those facts led to an effort for developing fiber-optics systems and an adoption of those systems worldwide [1].

From the 1980s to 2000s substantial improvements were made. Those are divided into four distinct generations of lightwave systems. First commercially available systems are traced back to 1975-1980 using wavelength of operation of 0.8μm and GaAs semiconductors lasers. Their performance is a bit rate of 45 Mb/s while the maximum repeater spacing was 10 km [2]. Those represent what is now known as first generation. The second generation, quickly developed after the first, used InGaAs to switch to 1.3 μm operating in a spectral area where fiber loss is reduced at 0.5 dB/km and minimum dispersion. Combined with single mode fibers,

between 1980-1985 emerged performances around 2 Gb/s and spacing of approximately 50 km [3] [4]. Third generation decide to use wavelength at 1.55 μm for minimum silica fiber losses [5]. But was quite slow to become commercially available and only released around 1990. The performance reached 10 Gb/s and repeater spacing of 60-70 km [6]. However, tremendously important breakthroughs took place for the fourth generation. The first reason is that instead of using electronics repeater, optical amplification was introduced resulting in lower losses such as in Erbium-doped fiber amplifiers [7]. The second and capital one is the implementation of wavelength division multiplexing (WDM) combined to the initial time-division multiplexing (TDM) [8, Chapter 9]. From this point, systems are not anymore limited by the processing speed of electronic circuits for multi/demultiplexing. The implications for this new technology was the emergence of all optical long distance networks around the globe. Performances doubled every 6 month to 1 year as seen on figure. By 2001, systems with a bit rate of 10 Tb/s were created and network of several 10 000 km existed [9]. It was at this revolutionary stage in lightwave systems that the AWGs emerged as an essential component through the WDM. In the end, for the last 15 years, the increase in the spectral efficiency was made by using mainly two techniques. The digital coherent transmission using multi-level quadrature amplitude modulation (QAM) where both the amplitude and phase of the carrying signal are simultaneously modified and the orthogonal frequency division multiplexing (OFDM) technique which transmit parallel data on a significant number of subcarriers special optical pulses are also used [10] [11]. By 2010 , such implementations allowed NTT to reach 69.1 Tbit/s with a 80 km single fiber accompanied by 3 EDFA and Raman Amplificators [12]. While recent papers suggest a transmission beyond 10 Tbit/s for 1500 km fibers [10].

Nowadays, in our ultra-connected society, with the IoT (Internet of Things) which is the interconnection of physical object using the internet and the increase in number of users [13], appears an explosion in computing and traffic in network systems [14]. This phenomenon

can be observed on figure 1.1 and figure 1.2 with a compound annual growth rate (CAGR) of around 30% per year which means a multiplication by 10 per decade. Photonics systems therefore plays an ever growing role particularly for data interconnects in computing systems and high-speed data transmission in network systems. A constant need of improving photonics systems is then essential. However, in this goal of improving systems, new issues regarding silica-based photonics components came into sight:

- The miniaturization of components due to the low density of integration

- The Energy efficiency due to the poor material characteristics

- Performances (trade-off to the energy efficiency)
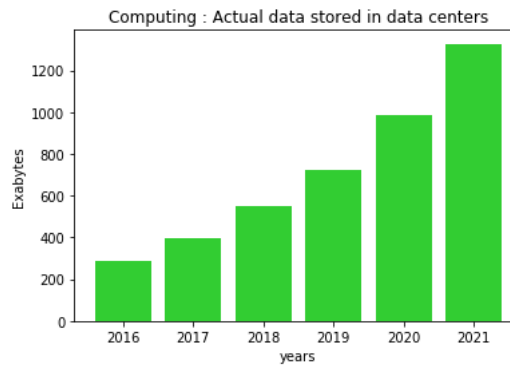
Figure (1.1): *Evolution of actual computing data stored in data centers through the years. Original data from cisco: [15].*
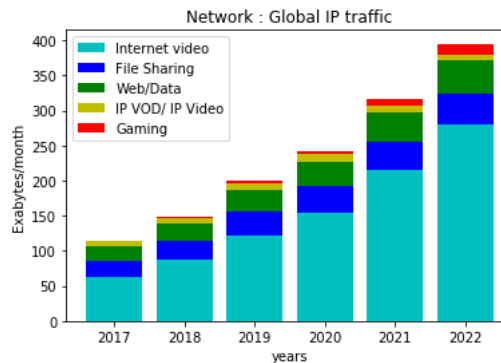

Figure (1.2): *Evolution of global IP traffic in networks and the part of use for each online application. Original data from cisco: [16].*

The solution found for partly overcoming those 3 silica problems, was found in using a new material for the core part of optical components.

The first reason being that Si photonics allows a better guiding mechanism in waveguide. Indeed, based on the situation described by figure 1.3 and using the following equation 1.1, the following observations can be made:

$$\theta_{r_{max}} = \cos^{-1}\left(\frac{n_{clad}}{n_{core}}\right). \tag{1.1}$$
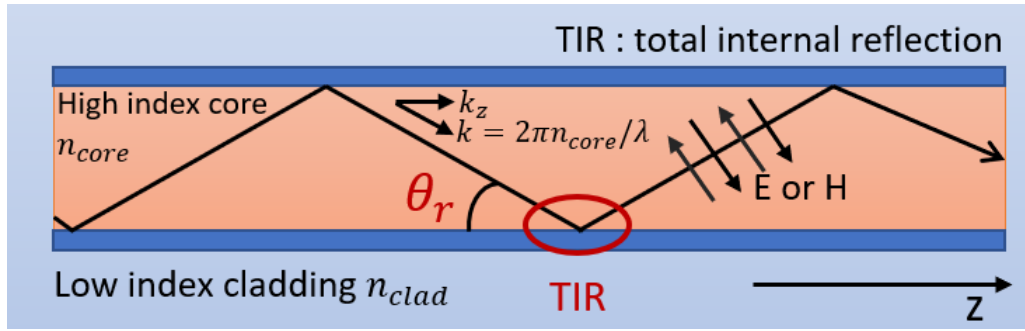
Figure (1.3): *Typical waveguide representation with core and cladding and light propagating through. As well representing the maximum acceptable angle of reflection.*

As $n_{Si} = 3.47$, $n_{SiO_2} = 1.44$, $n_{Ge/SiO_2} = 1.45$ for

- Ge-doped silica/silica :

$$\theta_{r_{max}} \sim 8 \; degrees \tag{1.2}$$

- *Si/SiO$_2$*:

$$\theta_{r_{max}} \sim 66 \; degrees. \tag{1.3}$$

Then, the acceptable angle of reflection being higher, the less power is carried out of the waveguide when the light is reflecting at the interface between the silicon core and the cladding made up using silica or other low index material. The second is a better optical

confinement. Effectively, the divergence angle of optical beams is determined is determined by the following equation :

$$\theta_b \sim \frac{\Delta k_x}{k} \sim \frac{1}{k\Delta x}.$$ (1.4)

From this equation follows the rule that a small optical beam Δx induces a larger divergence angle θ_b. The main point here is that this larger divergence angle can still be confined in silicon waveguides. Finally the third, and perhaps most important feature, is the higher density of integration of *Si* compare to *SiO$_2$* due to the high refractive index. The more Moore circuit principle both for core and bending is depicted on figure 1.6 [17]. This miniaturization induces many interesting consequences when combined with its CMOS compatibility. It allows multifunctionalities on a unique ship and cost effective production.
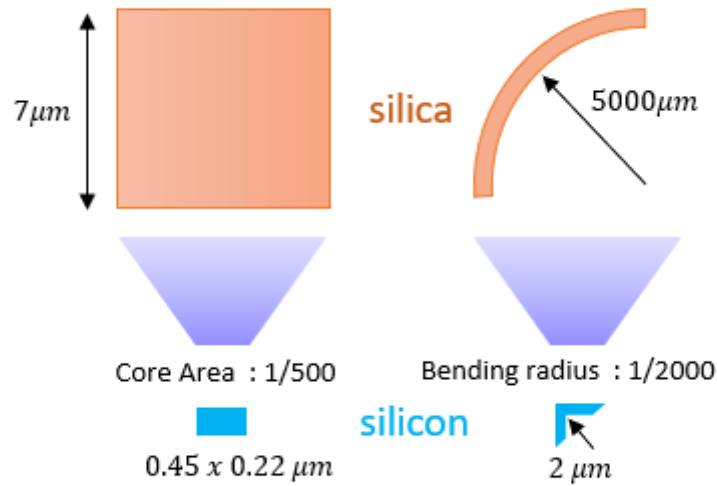
Figure (1.4): *Miniaturization comparison between silica and silicon components regarding both the core cross-sectional area and the bending radius dimensions.*

Both the widespread use of lightwave systems using WDM and the new solution of Si photonics to convey information more efficiently and faster led to the increase in the role of Si

AWGs in networks as these are used as wavelength multiplexers, demutiplexers and routers. The layout along with the demultiplexing properties of the AWG are represented on figure 1.5. Nevertheless, the Si photonics drawbacks come particularly into sight in geometrically complicated devices such as AWGs. Typically, because of the high refractive index difference in transition regions which induces larger phase error and scattering/losses [18]. The most sensible region located at the abrupt transition, with a high index difference between *Si* and SiO_2, between the planar slab region and the arrayed WGs region, which yields to optical field mismatch in addition to scattering.
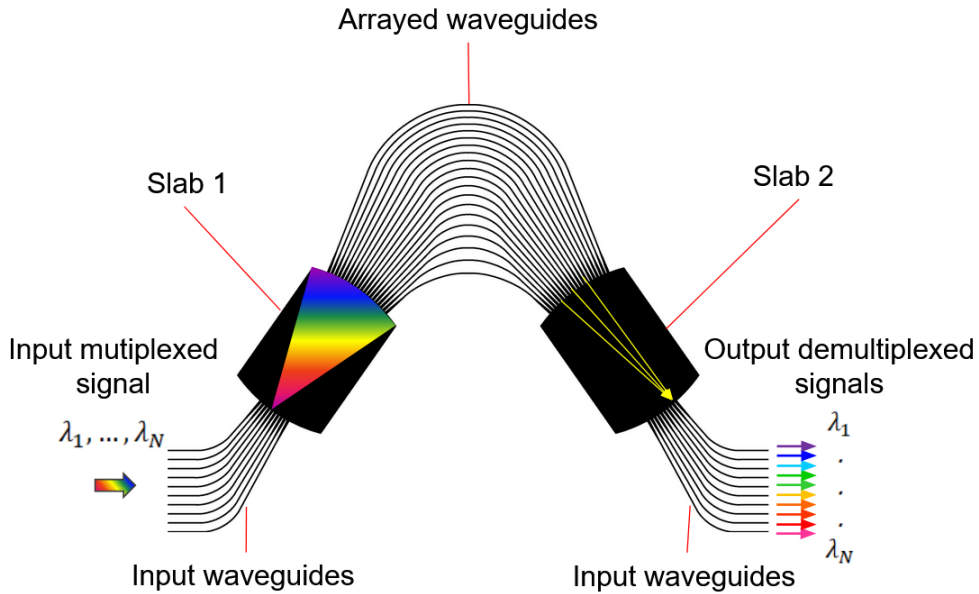
Figure (1.5): *Global view of the AWG with each part designed on the figure. It is accompanied by an illustrated view of the demultiplexing properties of the device. The input light contains many signals ranging from λ_1 to λ_N. It passes successively by the first slab, the array of waveguides and finally through the second slab to be demultiplexed in many individual colours $\lambda_1, ..., \lambda_N$, each propagating in an individual output waveguide.*

Under the perspective of decreasing the losses or phase error in optical networks, all the components must be subject to improvements. And the AWGs, being everywhere and numerous, are particularly subject to this last observation. Then, as explained in the above

paragraph, the importance of bringing improvements to the interface regions is prominent. Consequently, researches have tried to find a way to do so.

1.2 Notable AWGs applications

An AWG takes optical signals of different kinds as an input and can either be used for decomposing the signals into single wavelengths, each of those carrying a particular power or information. It can also perform the opposite operation of concatenating the signal (multiplexing) into a single or several signals each carrying a set of information. For this ability of performing multiplexing or demultiplexing the component plays a key role in WDM devices.

The WDM, commercially available only since 1995 [19], is a kind of transmission of information for which the information is encoded in multiple, independent wavelengths. It typically allows to take advantage of the large bandwidth offered by fibers and initially permitted to overcome the limits of the time division multiplexing (TDM), around tenths Gb/s [20]. In TDM, the different information components encoded in time had to be transmitted in different fibers. Instead, WDM multiplexes the different information in the same fiber but at different slots of the wavelength domain making it possible to reach several tenths of Tb/s. A schematic of the global structure of a WDM point-to-point link is shown on figure 1.6. The signals from transmitters are multiplexed, sent in the link, demultiplexed and find their respective receivers. This scheme then reflects why AWGs appear as important building block.
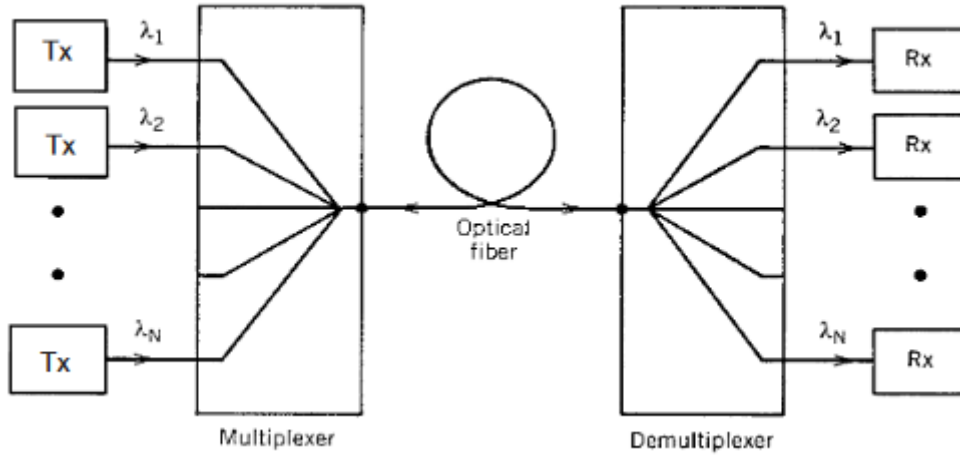
Figure (1.6): *Transmitter to receiver link showing the effect of multiplexing independent wavelength information in single fiber. Pictures used from : Agrawal, G. P. (2012). Fiber-optic communication systems (Vol. 222). John Wiley & Sons.*

As AWGs is included in the larger view of WDM, some high level requirements will impose values or constraints in design parameters one can possibly choose. A direct limiting factor from WDM on AWGs is how well one can divide the wavelength spectrum in smaller portion. This quantity is called the *channel spacing* Δv_{ch}. Another one is the *crosstalk* which should be below -20 dB. So that channel don't interfere with each other, it results from power leakage from one channel with the others [1, Chapter 8]. Also the *Loss nonuniformity* to make sure some components are not discriminated compare to others. Those WDM high level requirement imposing values will be explained and tabled in chapter 2.

A first and straightforward example is the use of AWGs as a simple multiplexer to send initial information into the networks or, to decompose the signal at the end of it and part the information between the various receivers [21]. A second use of AWGs for is for spectroscopy. Indeed, it is used to separated the individual wavelength component of the signal detected by the spectrometers. With each channel corresponding to an individual wavelength, encoded in

advance, it is then quite easy to determine the signal's composition [22] [23]. And finally, yet another example, is the use of N x N AWGs for building wavelength router [8, Preface].
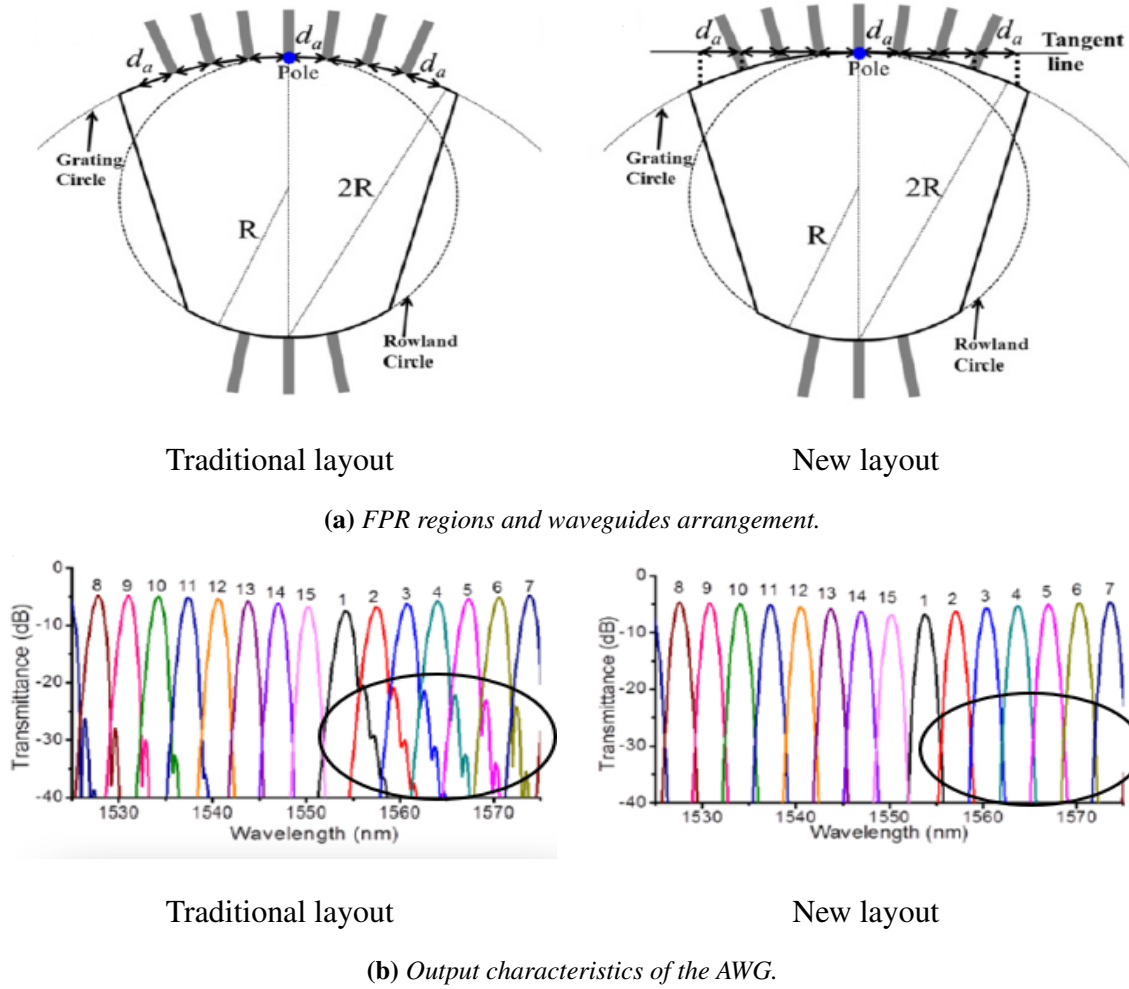
1.3 Previous Researches

In order to improve the silicon AWGs characteristics previous researches have used several techniques based on 3 main principles. The first one by modifying the fabrication techniques while switching to silicon photonics. But then, more extensively, the focus was put on two other methods. Those consist in introducing modifications on one of the constitutive parts of the AWGs. Either by intuitive or mathematical geometrical modifications changing the light propagation properties in one of the AWGs' components. Or by numerical methods which tend to compute the field profile by an iterative method such as beam propagation method (BPM) or the finite-difference time-domain (FDTD).and then modify the refractive index distribution to obtain a gain in the transmission profile. The most notable advances, from which some ideas for this study emerged will be presented and commented in the following paragraphs.

The modification in fabrication techniques, such as the lithography properties, can introduce notable upgrades in the AWGs output characteristics. For instance, as a brief example, *Pathak, Shibnath, et al.* investigated the "Effect of Mask Discretization on Performance of Silicon Arrayed Waveguide Gratings" to see how the variation in the length of the delay lines (waveguide array) was influencing the overall crosstalk. They concluded the possibility to an improvement from 2.7 to 6 dB in crosstalk and 1.2 to 5.0 dB in cumulative crosstalk by decreasing the mask grid from 5 nm to 1 nm [24]. Although, as these advances are dealing more with lithography or material modifications than AWGs modifications themselves, it will not be further explained as this does not concern the study of this research.

To begin with the recent research influencing ours, some geometrically modified part of the AWGs will be introduced. Those improvements consist of modifying the following : the regions where waveguides are bent, the waveguides themselves, the waveguides arrangement along the focal regions (where the field is focalized by the free propagation regions) or the transition region using single etching, double etching and/or tapered structures.

As a first example of modifications, regarding the waveguide arrangement, *Zou, Jun, et al.* proposed a structure where the arrayed waveguide were not disposed with a constant pitch on the focal ellipse of the free propagation region (FPR) but rather with a constant projected period on a line tangent to the grating at its pole. This, in order to reduce the aberrations, i.e. the crosstalk at the output. Effectively, as the Si waveguides exhibit sub-micron dimensions, even slight variations in their size will highly modify the propagation constant. This will change the optical path between the different waveguides in the FPRs and thus result in a high cross talk level. This method is diplayed on figure 1.7 (a) while the theoretical results are seen on 1.7 (b). Sensible improvement were demonstrated as performances drastically improve for both the theoretical case and its confirmation by experiments [25].

Traditional layout   New layout

(a) *FPR regions and waveguides arrangement.*

Traditional layout   New layout

(b) *Output characteristics of the AWG.*

Figure (1.7): *(a) Fabrication principle for the waveguide arrangement for two different layouts. On the left, using the traditional technique of a constant pitch along the grating circle while on the right, the new technique where the waveguide are disposed by projection from distances equally spaced on the tangent line to the grating circle and at its pole. (b) Output characteristics of the two layouts. On the left, the traditional output with the output aberrations circled while on the right, with the new layout the circle shows that those aberrations were successfully removed. Pictures used from : Zou, J., Le, Z., Hu, J., & He, J. J. (2017). Performance improvement for silicon-based arrayed waveguide grating router. Optics express, 25(9), 9963-9973.*

As a second example, several researches have focused on improving the transition of light between sensitive regions, where most of the loss or scattering comes form. This means guaranteeing an adiabatic transition for light from FPRs to waveguides and inversely, at the same time as minimize the length. The first techniques, for loss reduction, is based on the

famous paper by *Burns, WK and Milton, AF and Lee, AB* [26] and their coupling horns. Their main outcome is the development of the horns' width W for adiabatic transition. Using a ray model for the propagating light, and by stating that the adiabatic conversion condition is fulfilled when the half angle made by the taper width exceeds the angle between the ray and the axis of the channel (z), they obtained an equation for the required width W. From this new outcome of tapers structures, several publications have been made by trying various taper shapes (linear, parabolic, exponential, ...) at the FPRs/WGs interface in AWGs [27] [28]. The second techniques, dealing this time with suppressing multi-mode generation and scattering reduction, is the use of etching between the arrayed waveguides either as a single or a double process. *Park, Jaegyu, et al*, who added to conventional linear tapers structures a super-shallow etched region were able to have a low insertion loss of 0.63 dB and cross talk levels from -23 dB to -25.3 dB on fabricated devices [29]. *Okayama, H., et al* also used a similar process [30].

At last, the ultimate modifications to break through the trade-off between the size and performance of silicon components, is the use of various numerical optimization methods. These methods are designed to modify the Si refractive index distribution of sections of the devices, relatively to the surrounding material (resulting in a modifications of the boundary between the two materials). Several tools are required to do so. Primarily, an algorithm to compute the propagating field is used like the beam propagation method (BPM) or the finite-difference time-domain (FDTD). Then a figure of merit is defined, mostly based on the fields and geometrical parameters, eventually constraints. And finally a particular technique for renewing the index distribution is employed. At the end, the device is optimized with an unusual and often unpredictable shape but exhibits lower losses and cross-talk than manually optimized devices [31–35]. As a great and recent example, *Sawada, Yusuke, et al.* matured and ameliorated the wavefront matching method (WFW) using the formalism based on BPM for silica waveguide [36] to build a new 3-D finite element method (FEM) and apply it to Si-wire mode converters. The WFM scheme is presented on figure 1.8. The blue forward

propagating wave and the red ideal output wave coupling is improved at each iteration of the algorithm to enhance the global transmission of the Si-wire mode converter.
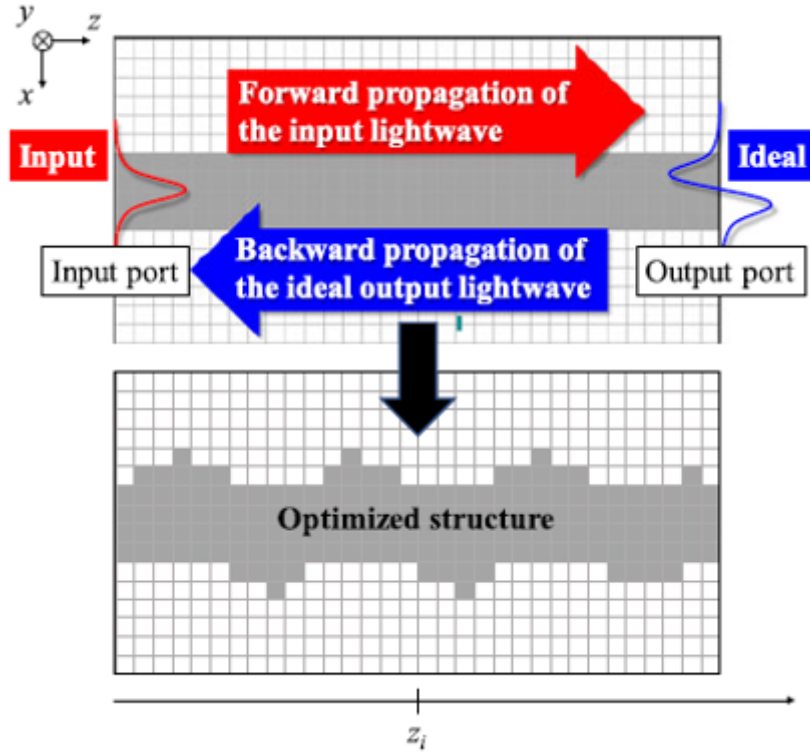
Figure (1.8): *The concept of the WFM method based on the FEM for waveguide discontinuity problems. The small grey square constitute the Si waveguide core while the white square represent the cladding. Their distribution is changed to improve the coupling between the forward propagating arbitrary wave used by the device (in blue) and the idea output wave (in red).Pictures used from : Sawada, Y., Sato, T., Fujisawa, T., & Saitoh, K. (2018). Development of the wavefront matching method based on the 3-D finite-element method and its application to Si-wire mode converters. Journal of Lightwave Technology, 36(17), 3652-3659.*

To conclude this section, this research summary highlights the particular importance of carefully designing the interfaces of the transition regions using the appropriate geometries and etching types. As well as the capability to do the work both intuitively by a physically or mathematically defined structure, supposed to introduce amelioration, or by an automatic iterative method based on the computation of the fields and the renewal or the refractive index distribution in a way or another. A good idea would be to eventually successively apply those

two methods. However, one must add that it is also important to find a trade-off with the length of the devices as well as its complexity in terms of the different parameters present in the optimization process as those dramatically influences the simulations complexity, the lithography complexity or even the tolerance of the device to fabrication errors. The previously designed AWG reported in this section are listed in table 1.1 along with the techniques used and the operational characteristics. Also the other additionnal methods used in Si photonics are gathered and shown in table 1.2.

Device	Loss (dB)	Crosstalk (dB)	Improvement technique	Remark	Reference
Silica AWG, 32 channels, 50 GHz	4 to 7	-60 (Theoretical)	Conventional AWG	Large footprint (mm^2)	*Doerr, Christopher Richard, and Katsunari Okamoto.*
Si AWG, 8 channels, 400 GHz	2.3 (5nm) $\to$ 1.3 (1nm)	-20 $\to$ -26	Lithography discretization 5nm $\to$ 1nm	Small footprint (mm^2) but harder to achieve	*Pathak, Shibnath, et al.*
Si AWG, 15 channels, 400 GHz	3.5	-19	Waveguide arrangement determined by tangential projection	Small footprint (mm^2) but sensitive to fabrication errors and etching type	*Zou, Jun, et al.*
Si AWG, 8 channels, 400 GHz	0.63	-23 to -25.3	ultrashallow etching	Footprint 400 $\times$ 240 μm^2 (small) but hard to manufacture	*Park, Jaegyu, et al.*

Table (1.1): *Summary table of the various previously designed AWG with the technique corresponding to the improvement and the operational characteristics*

Device	Loss (dB)	Crosstalk (dB)	Improvement technique	Remark	Reference
Si-wire mode converter	-0.56	NA	WFM based on 3D FEM	Very low reflections but time consuming process	*Sawada, Yusuke, et al.*
Various Si photonics devices	below -0.5	NA	Hierarchical 2 step gradient optimization under constraints	Long and tedious process and time consuming, local optimum	*Michaels, Andrew, Ming C. Wu, and Eli Yablonovitch.*

Table (1.2): *Summary table of the various previously designed Si photonics with the technique corresponding to the improvement and the operational characteristics*

1.4   Motivation, focus and objective of this study

Altogether, the research presented push toward transmission characteristics improvement of mainly loss even though crosstalk and loss variation are also accounted for. This is within the framework of using Si photonics to deal with the challenges of data transmission growth at the same time as the reduction of circuits' footprint. These studies all have in common the deals with geometrical modified structures but accomplish this objective in different ways.

In line with the previous observations, this thesis focus on using Si to build a simulated AWG part by part. Each part simulated with the appropriate tool to guarantee both time

efficiency and minimize the approximation compared with the actual operating device.

The main focus will be to particularly take care of improving the most sensitive region located at the interface between the slab (FPR) and the waveguide array and improve the transmittance. A good idea is to successively apply two cascaded optimization methods. The first one will consist in a geometrically defined topology optimized by :

- Combination of highly efficient components and shape to guarantee adiabatic transition at the FPR/WGs interface

- Optimization of these shapes' geometrical parameters to achieve better transmission

The second one is to include a slab etching process to reduce the impedance mismatch between regions with large difference in the refractive index.

The final objective of this study is therefore the comparison of the newly designed structure with a more simple, conventionally used one and evaluation of the overall characteristics of an AWG from its input to the output. All of this with parameters values being adequate to WDM system requirements.

The following chapter will thus concentrate on the operation of the AWG both physically and mathematically. Also will be described the components used in the first optimization method and the parameters that can be optimized.
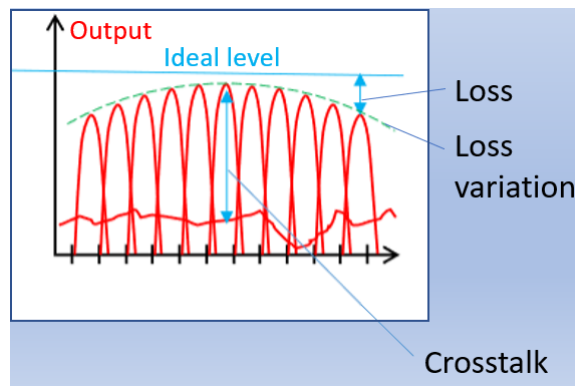
Figure (1.9): *AWG trasmission characteristics to optimize along with respecting high-level WDM system requirements. Pictures used with permission from : Tsuda H. Keio University.*

Chapter 2

Arrayed Waveguide Grating

The research for increasing transmission in the past decades resulted in the switch to optical fibers technologies and planar lightwave circuits (PLC) as those were major breakthrough for low-loss, compact networks. AWGs, emerging from this first new silica based PLCs technology, have started to be practically deployed in optical based networks in the middle of the 1990s. Since then, their performances and also functionalities have drastically improved since the beginning of the 21th century, notably because the switch to Si core material [8]. Their use has also been boosted by its small cost and high productivity due to its single mask technology. The AWGs are particularly interesting as those act as multiplexer/demultiplexer or routers in optical WDM devices, making it feasible to increase the overall capacity of each single fiber. AWG use Fourier Optics properties of diffraction performed by the FPRs regions and a phase-array of waveguides with constant phase delay, length designed such that it will result in the required imaging and dispersive properties at the output [37]. To make it simple it is an imaging device, taking as an input a single signal that may contain several individual wavelength and image those wavelength, or distribute, onto a spatial sequence of successive output arrays. The opposite is also true, i.e. from many individual wavelength the save devices perform the accumulation (or multiplexing) into a denser signal.

2.1 Theoretical principle of operation

In what follows, the layout will be presented, followed by the AWG propagation characteristics in each regions. This development is largely based on [37], [38] as well as [8]. Fourier optics will be used and sometime approximation on the field characteristics will also be made. The goal here is to obtain concise equation of the field in each region. This is useful for simulating the light transmission characteristics in some sections of the device. Notably, the important results are framed. Cases wherein the approximation is too far from the real propagation phenomena, i.e. for the FPR/AWs regions, will be treated by more sophisticated algorithms such as FDTD.

2.1.1 Layout and principle of operation
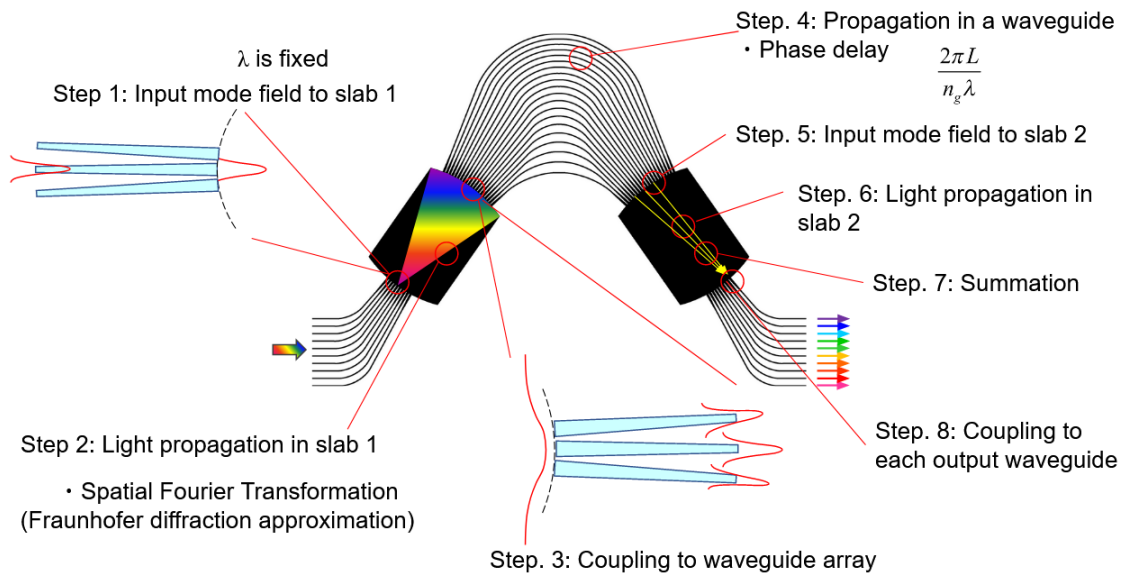
Figure (2.1): *Global view of the AWG with each successive transformation undergone by the input light ranging from step 1 to step 8. Those operation include diffraction, coupling to AWs, dephasing, and coupling to the second slab where the final output is a a summation of field spatially distributed along the second FPR/output waveveguide interface therefore demultiplexing the input field.*
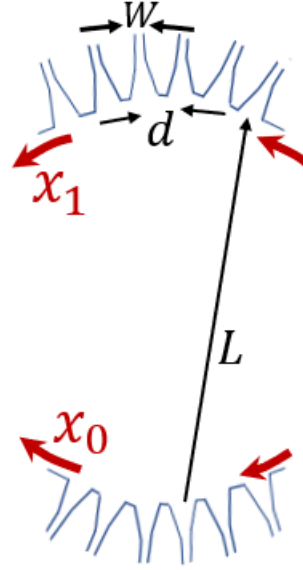
Figure (2.2): *The first FPR region with the waveguides axis x_0 and x_1, where the light enter the first FPR and where it enters the waveguide array, respectively. Also the length L of the FPR, the distance between waveguides d and the waveguide width W are displayed.*

The constituents of the AWs were previously presented on figure 1.5. The new AWGs layout, as seen on figure 2.1, describe the 8 successive operation the AWG performs on an arbitrary incoming light. It consist of input waveguides feeding the incoming light into the first slab or free propagation region. Then, arrayed waveguides, with a constant increment in their length by a fixed factor Δl, receives the diffracted light form the first FPR. This array behaves as a phase array. As each individual signal carried in each individual waveguide travel a difference distance, their phases will all be different when coming out of the phase array. This phase difference property, allows the signal to constructively and destructively interfere in the second slab at the interface with the output array. The important geometrical parameters are the *waveguide spacing d*, the waveguide *width W*, the *length of the FPR L*, corresponding to the radius of curvature over which the waguides are disposed, and the *gap between waveguide g*.

2.1.2 Input and first FPR

The first FPR scheme is displayed on 2.2. It has to be noted that the input waveguide axis is denoted x_0 and the FPR/AWs interface axis is name x_1.

At the entrance of the FPR region, the field coming from an external source has profile :

$$f(t,x_0) = u(t)e^{i2\pi v_0 t}f_0(x_0). \tag{2.1}$$

This field is therefore varying temporally but also as a spatial profile, here distributed along the x_0 axis. In the frequency domain it takes the form :

$$F(v,x_0) = U(v - v_0)f_0(x_0). \tag{2.2}$$

This field distribution is radiated through the FPR regions and cross it. Using Fourier optics we can compute the diffraction pattern. The Fourier Transform of the spatial distribution will give the resulting field along the x_1 axis. Considering the field is traveling far enough and therefore using Fraunhofer approximation with limitig criteria

$$L \gg \frac{\pi W^2}{4\lambda} \tag{2.3}$$

which in the particular case of our design with waveguide width W = $0.45\mu m$ and wavelength values $\lambda = 1550$ nm. The approximation is valid as soon as $L \gg 0.1\mu m$. From Fraunhofer's formalism, the spatial Fourier transform on the observation plane becomes :

$$f(x_1) = \frac{1}{\sqrt{\alpha_v}}\mathscr{F}\{f_0(x_0)\}|_{u=x_1/\alpha_v}. \tag{2.4}$$

As above-mentioned, this is a spatial Fourier transform, not a Fourier transform resulting form a transformation of the time domain. To be clear, we define u as the spatial frequency domain variable as opposed to v the frequency domain variable. In equation 2.4, the fraunhofer

integral is defined when we write the resulting coordinate plane as a function of the angle of observation $\theta_{x_1} = x_1/L$, angle under which we see the obstacle. Therefore, the variable $u = \frac{\theta_{x_1}}{\lambda}$ [39, 40]. The factor α_ν is then the product of wavelength and the focal length in Fourier optics propagation, the wavelength in the slab being λ/n_s with n_s the slab index :

$$\alpha_\nu = \frac{cL}{n_s \nu} = \frac{\lambda L}{n_s}. \tag{2.5}$$

This factor can be approximated as a constant since the signal components are very close to each other in the frequency domain. Accordingly, the approximation as a function of the central frequency of the spectrum gives $\alpha_\nu = \alpha_{\nu_0} = \alpha$.

At the present, to compute an analytically defined shape of the spectrum arriving at the interface with the waveguides, the form of the input propagating beam must be defined. It is thus stated that the signal coming from the central input waveguide is a gaussian normalized profile. This is reasonable while utilizing single mode input waveguides carrying gaussian beams for the input array.

$$b_i(x_0) = \sqrt[4]{\frac{2}{\pi \omega_i^2}} e^{-(x_0/\omega_i)^2}. \tag{2.6}$$

The subscript i stands for the "input". The quantity ω_i is the mode field radius of the input waveguides. Combining equation 2.4 and 2.6 gives the final shape striking the waveguide array inputs:

$$B_i(x_1) = \sqrt[4]{2\pi \frac{\omega_i^2}{\alpha^2}} e^{-(\pi \omega_i(x_1/\alpha))^2}. \tag{2.7}$$

2.1.3 Transition regions between FPR and the AWs

At this sensitive interface of the device, an important quantity emerges : the overlap integral between the incoming field, illuminating the inputs of the waveguide array, and the waveguide

modes. Again, as in equation 2.4, the arrayed waveguide being composed by fundamental mode waveguides :

$$b_g(x_1) = \sqrt[4]{\frac{2}{\pi \omega_g^2}} e^{-(x_1/\omega_g)^2}. \tag{2.8}$$

The subscript g stands for the "grating". The quantity ω_g is the mode field radius of the waveguide grating. For the centered waveguide, for which coordinate $x_1 = 0$, the illumination or overlap integral a from the incoming field that actually excites the fundamental mode is

$$\boxed{a = \int_{-\infty}^{+\infty} B_i(x_1) b_g(x_1) \partial x_1}. \tag{2.9}$$

This quantity is an energy. And to go further, by supposing the illumination as constant over the entire waveguide width. It means, by fulfilling the condition

$$\frac{\pi \omega_i}{\alpha} \ll \frac{1}{\omega_g}. \tag{2.10}$$

The term B_i becomes a constant and can be taken out of the integral equation 2.9. Thus only the term $b_g(x_1)$ is integrated over the x_1 boundary.

$$a \simeq \sqrt[4]{2\pi \omega_g^2} B_i(x_1 = 0) \tag{2.11}$$

Now instead of considering only the centered waveguide, the equation is written for the global interface, each waveguide spaced by a distance d.

$$f_1(x_1) = \sqrt[4]{2\pi \omega_g^2} \sum_n B_i(nd) b_g(x_1 - nd) \tag{2.12}$$

From this point, if the number of waveguides N is set, and as usual considering the centered waveguide as reference for $x_1 = 0$. Equation 2.12 can be rewritten even more precisely. It is also useful to write it in a form more suitable for simulation purpose.

$$f_1(x_1) = \left[rect\left(\frac{x_1}{Nd}\right) B_i(x_1)\delta_d(x_1) \right] * \sqrt[4]{2\pi\omega_g^2} b_g(x_1).$$ (2.13)

Where $*$ is the convolution product, $\delta_d(x_1) = \sum_{r=-\infty}^{+\infty} \delta(x_1 - rd)$ and *rect* is the rectangular function, here defined as :

$$rect\left(\frac{x_1}{Nd}\right) = \begin{cases} 1, & |x_1| \leq \frac{Nd}{2} \\ 0, & \text{otherwise} \end{cases}.$$ (2.14)

2.1.4 Field traveling in the AWs

Sampled copies of the field have now entered each individual waveguide in the grating. However, each waveguide has a different length consequently, each copy will be subject to a different dephasing. This part is dealing with phase change in the signals at the end of the grating.

$$l_n = l_0 + \Delta l(n + \frac{N}{2})$$ (2.15)

Here, we defined the length difference *Deltal* between each consecutive waveguide. The shortest waveguide at $n = -N/2$ will then have length l_0 and the longest at $n = N/2$ length $l_0 + N\Delta l$. *Deltal* has to be an integer of the operation wavelength, this will allows to have the emitted light from the central input waveguide to focus exactly at the central output waveguide (at the interface between the second FPR and the output waveguides).

$$\Delta l = \frac{m\lambda_0}{n_g} = \frac{mc}{n_g v_0}$$ (2.16)

m is called the grating order and n_g is the refractive index of the arrayed waveguides. The simple length increment Δl increases the phase by

$$\beta \Delta l = 2\pi m \frac{v}{v_0}.$$ (2.17)

Similarly, the entire distance increases the phase by

$$\Delta\phi_n = \beta l_n = 2\pi \frac{n_g}{c} v_g.$$

(2.18)

Figure 2.3 shows the configuration of the second slab, free propagation region between the arrayed waveguides and the output waveguides. x_2 refers to waveguide axis. The field at this interface becomes
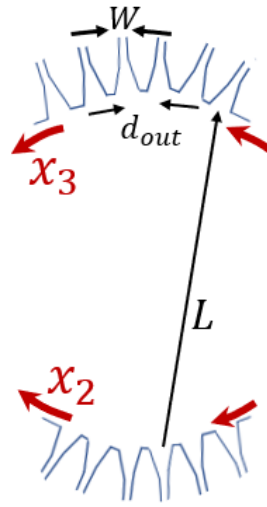
Figure (2.3): *Second FPR where the field comes out of the arrayed waveguide at the level of the axis x_2, to be spatially focused on the output waveguides at the interface represented by the axis x_3*

.

$$f_2(x_2) = \left[rect\left(\frac{x_2}{Nd}\right) B_i(x_2)\delta_d(x_2)\phi(x_2,v) \right] * \sqrt[4]{2\pi\omega_g^2} b_g(x_2).$$

(2.19)

For the sake of clarity in the equation the phase term was condensed into $\phi(x_2,v)$. In reality, phase delay acting on a given signal is nothing else than the multiplication of the signal with a complex exponential. Thus the signal in equation 2.13

$$\phi(x_2,v) = e^{-i\Delta\phi_n}.$$

(2.20)

If the right term of equation 2.20 is developed, it ends up in a formula that can be divided into 2 terms. One as a function of only v and the other of both v and x_2. This formulation will be important for the section next mathematical operations of the field. Then

$$f_2(x_2, v) = \boxed{\left[B_i(x_2)rect\left(\frac{x_2}{Nd}\right)\delta_d(x_2)\phi(x_2, v)\right] * \sqrt[4]{2\pi\omega_g^2}b_g(x_2)}. \qquad (2.21)$$

With

$$\phi(x_2, v) = \psi(v)e^{-j2\pi m(v/v_0)(x_2/d)}, \qquad (2.22)$$

$$\psi(v) = e^{-i2\pi v((n_g L_0/c)+(mN/v_0 z))}. \qquad (2.23)$$

2.1.5 Second FPR and output waveguides

In a similar way as in the first section, to obtain the field at the interface between the second FPR and the output waveguides the Fourier optics method is repeated. The field arriving to the waveguide is the Fourier Transform of the field output by the grating array and again, the Fraunhofer approximation is used.

$$f_3(x_3, v) = \frac{1}{\sqrt{\alpha}}[b_i(x_3) * \text{sinc}\left(Nd\frac{x_3}{\alpha}\right) * \Delta_d(x_3) * \Phi(x_3, v)]\sqrt[4]{2\pi\omega_g^2}B_g(x_3) \qquad (2.24)$$

To obtain this quite complicated expression, it is useful to recall that the Fourier transform operation can be done on each individual terms and the operations of multiplication and convolution in one domain become the convolution and mutiplication in the other domain, respectively. The mathematical operations and the various terms resulting from, all evaluated at $F|_{u=x_3/\alpha}$, are :

- The Fourier Transform of a Gaussian is also a Gaussian :

$$B_i(x_2) \xrightarrow{\mathscr{F}} b_g(x_3) = \sqrt[4]{\frac{2}{\pi \omega_i^2}} e^{-(x_3/\omega_i)^2} \tag{2.25}$$

$$b_g(x_2) \xrightarrow{\mathscr{F}} B_i(x_3) = \sqrt[4]{2\pi \omega_g^2} e^{-(\pi \omega_g (x_3/\alpha))^2} \tag{2.26}$$

- The Fourier Transform of the rectangular function is the sinus cardinal :

$$rect\left(\frac{x_1}{Nd}\right) \xrightarrow{\mathscr{F}} \text{sinc}\left(Nd\frac{x_3}{\alpha}\right) \tag{2.27}$$

- The Fourier Transform of the a comb of delta is also a comb of delta functions :

$$\delta_d(x_2) \xrightarrow{\mathscr{F}} \Delta_d(x_3) = \sum_{r=-\infty}^{\infty} \delta\left(x_3 - r\frac{\alpha}{d}\right) \tag{2.28}$$

- The Fourier Transform of a complex exponential is a delta :

$$\Phi(x_3, \nu) \xrightarrow{\mathscr{F}} \phi(x_2, \nu) = \psi(\nu)\delta\left(x_3 + \frac{\alpha m}{d\nu_0}\nu\right) \tag{2.29}$$

Equation 2.24 can be more precisely analytically described by convoluting all the terms sequentially giving

$$\boxed{f_3(x_3, \nu) = \sqrt[4]{\frac{2\pi \omega_g^2}{\alpha^2}} B_g(x_3)\psi(\nu) \sum_{n=-\infty}^{\infty} f_T\left(x_3 - n\frac{\alpha}{d} + \frac{\nu}{\gamma}\right)}. \tag{2.30}$$

Where the convolution $b_i(x_3) * \text{sinc}(Nd\frac{x_3}{\alpha})$ is a very special mathematical quantity. Actually it is the Fourier transform of a gaussian function truncated by a rectangular function. It cannot

be solved exactly by a simple unique form. The name of the solution is called f_T, T for "truncated", and deals with erf function such that

$$f_T(x_3) = \left(\frac{\alpha^2}{8\pi\omega_i^2} \right)^{1/4} e^{-(x_3/\omega_i)^2} \left[\text{erf}\left(\frac{\pi\omega_i Nd}{2\alpha} + i\frac{x_3}{\alpha} \right) + \text{erf}\left(\frac{\pi\omega_i Nd}{2\alpha} - i\frac{x_3}{\alpha} \right) \right]. \quad (2.31)$$

From equation 2.30 it can easily be understood the relationship between the spatial axis x_3, and the frequency being distributes over it. Each function f_T is repeated for the individual frequency components ν. At which position the frequencies are repeated depending on several parameters, for a fixed value of n, d, alpha there is also the quantity

$$\gamma = \frac{d\nu_0}{\alpha m}. \quad (2.32)$$

Being the "frequency spatial dispersion parameter" (FSDP) which determines, when m is fixed, the places to put the output waveguides on the interface. Equation 2.30 is usually rewritten as

$$f_3(x_3, \nu) = \sqrt[4]{2\pi\omega_g^2} B_g(x_3) \psi(\nu) \sum_{r=-\infty}^{\infty} f_T\left(x_3 - \Delta x_{3,\text{FSR}} \left[n - \frac{\nu}{\Delta\nu_{\text{FSR},0}} \right] \right). \quad (2.33)$$

With

$$\Delta x_{3,\text{FSR}} = \frac{\alpha}{d_w} \quad (2.34)$$

the spatial free spectral range (SFSR), distance for which the same temporal frequency will be repeated by different diffraction orders m. And

$$\Delta\nu_{\text{FSR}} = \frac{\nu}{m} \quad (2.35)$$

the frequency free spectral range(FFSR) or FSR for which different frequencies are focused to the same port.

In order to obtain the very final formulation of the output waveforms for the AWG we use again the overlap integral method. The incoming field on boundary x_3 is overlapped with the fundamental mode of the output waveguide, along the width of this waveguide. This time for the light coming from the central input waveguide the illumination is

$$t_q(\nu) = \int_{-\infty}^{+\infty} f_3(x_3, \nu) b_{out}(x_3 - qd_{out}) \partial, x_3 \tag{2.36}$$

with q the output waveguide number, the output waveguide mode and d_{out} is the spacing between successive output waveguide. Generalizing from 1 input waveguide to a number p of waveguides, the different input waveguides modes are the same but switched spatially

$$b_{i,p}(x_0) = b_i(x_0 - pd_i) = e^{-((x_0 - pd_i)/\omega_i t)^2}. \tag{2.37}$$

Equation 2.33 also only one additional term of $+pd_i$

$$\boxed{f_3(x_3, \nu) = \sqrt[4]{2\pi\omega_g^2} B_g(x_3) \psi(\nu) \sum_{r=-\infty}^{\infty} f_T\left(x_3 + pd_i - \Delta x_{3,\text{FSR}}\left[n - \frac{\nu}{\Delta\nu_{\text{FSR},0}}\right]\right)}. \tag{2.38}$$

And the illumination on a particular output waveguide q, from a particular input waveguide p, being the final all in one frequency response is

$$\boxed{t_{p,q}(\nu) = \int_{-\infty}^{+\infty} f_{3,p}(x_3, \nu) b_{out}(x_3 - qd_{out}) \partial x_3}. \tag{2.39}$$

2.2 Modified sections

A careful study of what happens to the light beams in modified sections is particularly relevant regarding the first optimization procedure undergone by our device. As explained in the previous sections, this study focuses on the interface FPRs/AWs where light should ideally be converted in a perfect adiabatic manner and where scattering should be reduced as much as possible, i.e. we want to avoid both the backward reflections and power conversion in mode higher than the fundamental mode of the waveguides. The choice is made of assembling both tapers and rib waveguide. The first one for enhancing the light transition phenomenon the second one for reducing scattering to a minimum. Nevertheles, multiple alternatives exist for reaching en adequate structure. Our design will modify and optimize the interface by choosing the best combination among several alternative each of those previously optimized to guarantee an overall optimized conformation.

2.2.1 Tapers

An arbitrary taper shape can be observe on figure 2.4. For this kind of layout, it is essential to efficiently connect the large section to the narrow channel typically from the slab to single mode waveguides. As developed by *Burns, WK and Milton, AF and Lee, AB* [26], using ray optics to develop a model for adiabatic transition, the fundamental condition that needs to be satisfied is that, at each point, the semi-angle of the waveguide θ_h (h for "half")must be smaller than phase of the lowest order mode of the input beam inside the taper θ_p (p for "phase"). If this is not the case, and thus the progression of the spreading of the waveguide is faster than the phase θ_p, then energy is converted is higher order modes or radiation modes and distortion appears [27].
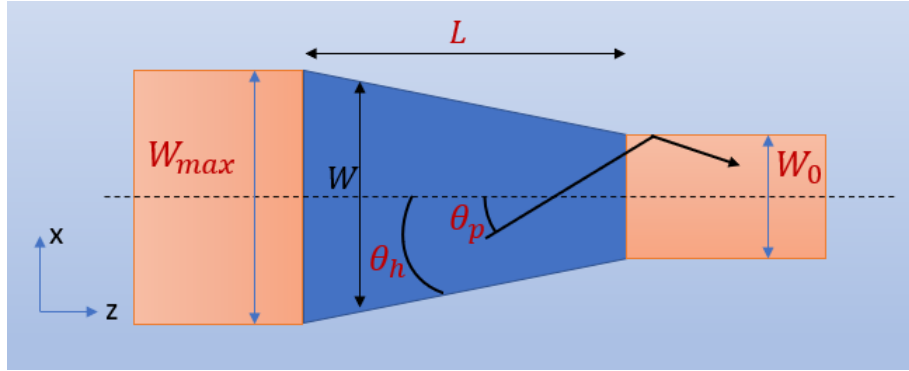
Figure (2.4): *Arbitrary taper for which the function of the W width has not yet been resolved, it is then displayed as a linear basic taper. The parameters are the initial width W_0 and the final width W_{max}. In our design the W_0 is the regular width of the input, output and arrayed waveguides while W_{max} is the width of the taper when projected in the slabs*

The condition can be written quite simply as

$$\theta_h(z) = \alpha \theta_p(z). \tag{2.40}$$

After development [26] and taking into account the desire of a minimized length, it can be written only as design parameter by

$$\theta_h < \frac{\lambda_0}{2W n_{\text{eff}}} \tag{2.41}$$

And as it is the half angle the condition on the width W is given in equation 2.42.

$$\frac{dW}{dz} = \alpha \lambda_0 / n_b W \tag{2.42}$$

As first approximation for the global equation enabling to solve for the distance is to suppose the effective refractive index to be the one of the bulk, the material used to build the taper, i.e. Si. The result displayed in equation 2.43 correspond to a parabolic taper.

$$\boxed{W^2 = (2\alpha \lambda_0 / n_b) z + W_0^2} \tag{2.43}$$

If this condition is not made the taper shape is not exactly parabolic but it stays a good approxi-mation. Researches have demonstrate it is the best candidate between several alternatives [28]. In our design, the effective refractive index is indeed varying between the beginning of the taper to its end. To approximate the ideal shape in a proper way, a parabolic function is used but its shape is tuned using a tuning parameter later called "d". An illustrated version of the parabolic tapers is produced on figure 2.5.
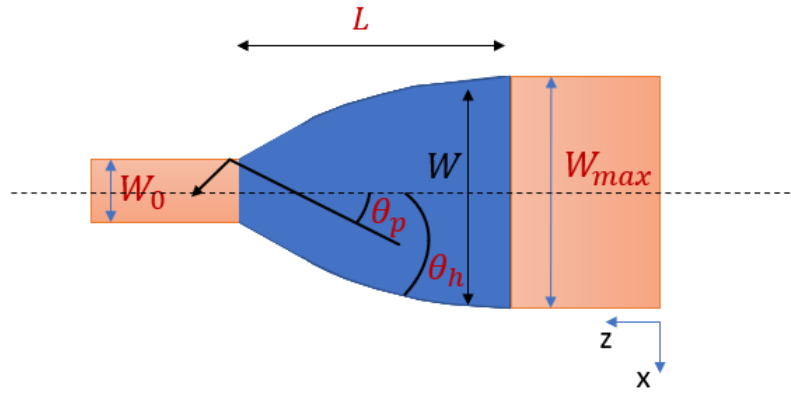
Figure (2.5): *Parabolic taper layout. The parameters are the initial width W_0 and the final width W_{max}. The slope of the parabola can be modified as well as the length L*

.

As a summary, the taper acts as a waveform converter between different part of a device where the waveform exhibit distinct behaviors. This phenomena can be observed for a linear taper arbitrary interface in figure 2.6 where the waveguide fundametal mode is broaden into a larger wavefront to be launched in a slab. Design rules have been developed and will be applied to simulate the device and particularly in the interface regions where tapers take all their significance. Regarding the exact choice of the optimization parameters and the metric determining the optimal values and general shape, it will be describe in chapter 4 dealing with simulation method, implementation and results.
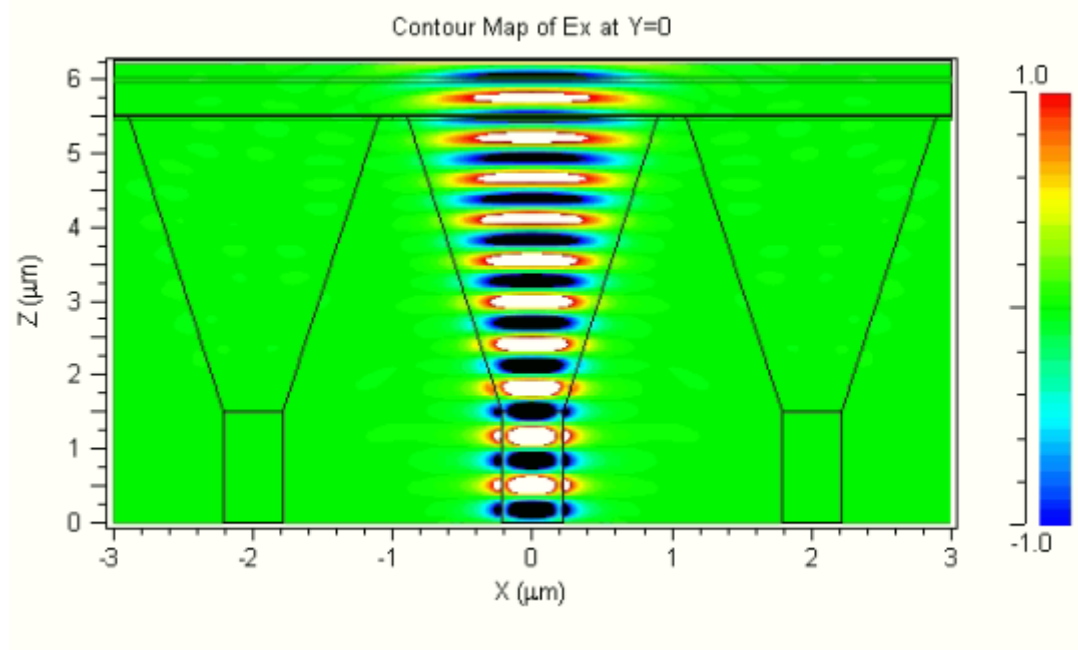
Figure (2.6): *Light propagation in linear taper transition interface using FDTD simulation and light propagating in the z direction. The electric field beam is enlarge as the light propagates from the input waveguide into a slab.*
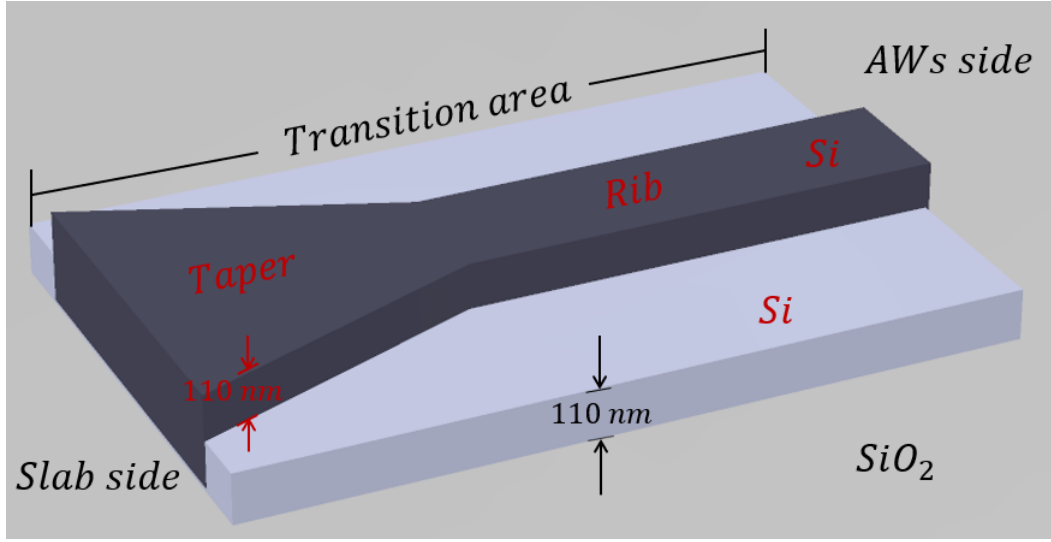
2.2.2 Rib Waveguide

Another element that will be considered and in which one must be particularly careful is its conception is the etched part between the arrayed waveguides and the rib waveguide resulting. This element is necessary for scattering reduction [29]. The goal is also to make sure that vertically, there is only the fundamental mode which travels through our transition region and reaches the fundamental mode waveguides of the grating array. This is in order to avoid more than one maximum in the vertical direction as the lowest maxima would couple to the slab modes an result in leakage. The condition to apply in this case, as already studied in [41–43] and given the configuration displayed by figure 2.7 is provided by equation 2.44. This is a theoretical approximation, however it is particularly true for low values of h/H [42, 43], i.e. $0.5 < h/H < 0.6$.
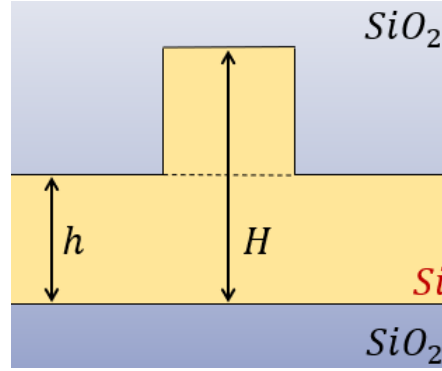
Figure (2.7): *Rib waveguide cross sectional area with a core composed of Si and a cladding composed of SiO$_2$. The height of the slab is h while to total height of the rib is H. The blue gradient in the background plane refers to the effective refractive index variation from the lower part of the slab to the upper part where it is lower.*

.

$$\frac{h}{H} \geq 0.5 \qquad (2.44)$$

In fact, half-etching was chosen for the design which allows the condition to be verified. Then the values for the parameters are h = 110*nm* and H = 220*nm*. H having the same height as the fundamental mode Si waveguide composing the waveguide array. An illustrated 3D view of a potential single element of our interface is shown on figure 2.9. On this picture both the taper, rib waveguide and the half-etching are highlighted.

Figure (2.8): *Example of a potential structure for the element composing the interface between the FPRs and AWs in the design. The taper and rib waveguide are highlighted as well as the half etching using h = 110nm and H = 220nm.*

2.2.3   Slab etching area

The final idea for modifications of the light profile at the interface is the etching taking place not only between the waveguides, previously mentioned and used in traditional design, but also in the slab, before the light couples into the tapers. The idea is to introduce irregularities to allow more degree of freedom on the system and tune the refractive index distribution. Those etching area will be arbitrarily set to be rectangular. Three different parameters are chosen for this approach : *detch* the distance between the etched areas and the waveguide array in the z direction (lightwave propagation direction), *letch* the length of the etched area in the z direction and *wetch* the width in the x direction (transverse lightwave propagation direction). The etching depth was not consider as a reasonable fourth parameter as the single-mask lithography process is limited in this direction. A simulated refractive index profile of an interface including this etching strategy is displayed on figure 2.10.
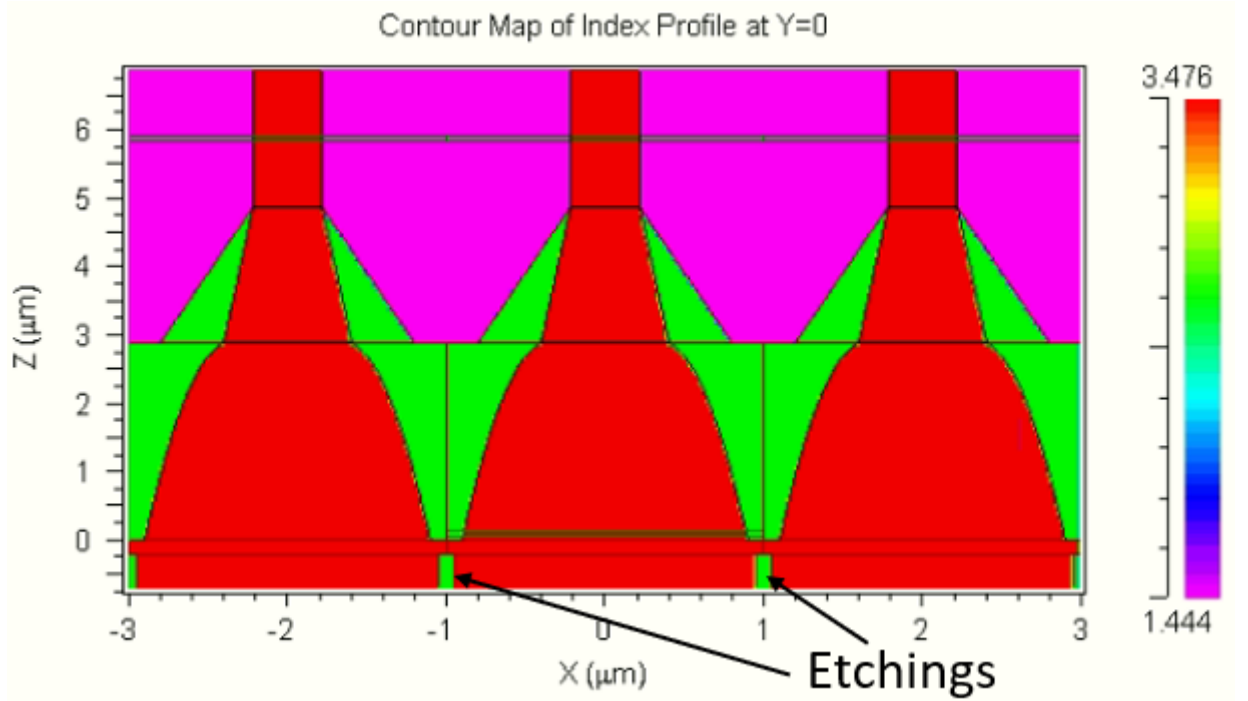
Figure (2.9): *Actual implemented interface between the FPRs and AWs in the design, using half etching with h = 110nm and H = 220nm. The cut is realized exactly at the middle of the perpendicular direction to the slab. Three distinct zone appear : the high n_{Si} zone in red, the low n_{SiO_2} zone in fuschia and the bright green zone with and intermediary index as it is exactly located at the boundary between the two previously quoted zones.*

2.3 Additional theoretical notions

Other more general notions are important to understand the mechanism of light propagation in a device such as the AWGs. Only the two main notions of the effective refractive index relative in a particular medium n_{eff} and the impedance mismatch between the different regions of the device will be explained. The main reason being that those two directly influence the transmittance of given waveguide structures.

2.3.1 Effective refractive index

In general, the effective refractive index of a medium, n_{eff}, is the ratio of the speed of light in vacuum to the speed of light to the speed of light traveling in this bulk medium, at a given frequency ω. Mathematically,

$$n_{eff}(\omega, \varepsilon_r, \mu_r) = \frac{c}{v} = \sqrt{\varepsilon_r(\omega)\mu_r(\omega)} \tag{2.45}$$

with ε_r, μ_r the relative permittivity and relative permeability, respectively. It is important to note that in most optical media the permeability is not modified relatively to the vacuum permeability such that $\mu_r = 1$ and then one will consider $n_{eff} = \sqrt{\varepsilon_r}$.

In planar waveguide structures (slab, rib waveguides, ...) the definition is slightly more complex as the refractive index is determined by the planar waveguide geometry and does not only depends on one material but several materials and on the propagating mode, as each mode have a different spatial profile. For the studied structure, the refractive index of a light propagating in the core region of the structure takes values such that :

$$n_{SiO_2} \leq n_{eff} \leq n_{Si} \tag{2.46}$$

where n_{SiO_2} is the refractive index of the cladding while n_{Si} is the refractive index of the core [8, Chapter 2]. An important notion is that n_{eff} is intimately linked to the idea of modes in a guiding structure. Effectively, each mode possesses its own effective refractive index. If both the wavelength and the geometrical parameters of the waveguide are known then for each propagating mode the propagation constant β can be obtained after solving Maxwell's equation [8, Chapter 2]. Therefore what is called the effective refractive index is given by

$$n_{eff} = \frac{\beta}{k}. \tag{2.47}$$

The reader should observe that different modes posses different values for β and then different effective refractive indexes.

Another important point is the *cutoff* condition, i.e. the geometrical values of waveguides from which the structure allows the propagation of higher modes than the fundamental mode. For rib waveguides, by defining the normalized frequency V by

$$V = k_0 a \left(n_{Si}^2 - n_{SiO_2}^2 \right)^{1/2} \tag{2.48}$$

where the width of the rib is 2a. And the normalized propagation constant

$$b = \frac{n_{eff}^2 - n_{SiO_2}^2}{n_{Si}^2 - n_{SiO_2}^2}. \tag{2.49}$$

In addition, by taking the Maxwell's equations solutions and rewritting the dispersion equation by

$$V\sqrt{1-b} = \frac{m\pi}{2} + \tan^{-1}\sqrt{\frac{b}{1-b}}. \tag{2.50}$$

with m the mode order. There is a particular value for V which is the *cutoff* condition [8, Chapter 2]. Below this value, the waveguide allows propagation of the fundamental mode with m = 0 and above the higher orders ones.

To summarize everything at once, what can be deduced from the above discussion is that if, along with the direction of propagation of the light Z, the material distribution is modified, or equivalently the refractive index distribution is modified, then because the n_{eff} will be modified thus the parameter V is also modified. Therefore, there is a risk of obtaining a value of V above the cutoff condition in the optical waveguide. Again, as this particularly happens at regions where the refractive index distribution is modified, the interface slab/arrayed waveguide in AWGs is particularly sensitive to undesired multimode generation. Those multimode are mostly just losses or induce a diffusion and as a result the transmittance

is reduced and the crosstalk increases. Thus it is important to implement the previously
mentioned technique such as special etching for suppressing multimode generation.

Several researches have already studied the geometrical values of Si waveguides (height and
width) corresponding to the cutoff condition. Those are the height of 220 nm and a width
below or equal to 450 nm [44].

2.3.2   Impedance mismatch

When light propagates between two media having two different refractive index, called n_1
and n_2. At the interface between the two media, a part of the wave is transmitted while the
other part is reflected. Considering the situation on figure 2.10, the amplitude coefficient for
transmission and reflection are given by equation 2.49 [45].
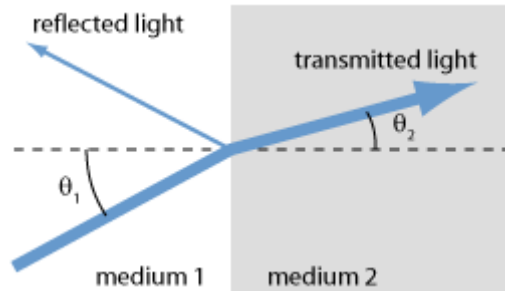
Figure (2.10): *Reflection at the interface between two media with different refractive index.
Pictures used from :* `https: // www. rp-photonics. com/ fresnel_ equations. html`

$$t = \frac{2n_1 \cos \theta_1}{n_1 \cos \theta_1 + n_2 \cos \theta_2}$$
$$r = \frac{n_1 \cos \theta_1 - n_2 \cos \theta_2}{n_1 \cos \theta_1 + n_2 \cos \theta_2}$$

(2.51)

If we are just interested in the a ray of light at normal incidence, corresponding to the light
wave traveling in the z direction of the AWG the equation is rewritten by equation 2.51.

$$t = \frac{2n_1}{n_1 + n_2}$$
$$r = \frac{n_1 - n_2}{n_1 + n_2}$$
(2.52)

And the power reflected due to the mismatch of the 2 indexes or equivalently the impedance mismatch of the two media is shown in equation 2.52.

$$R = \left(\frac{n_1 - n_2}{n_1 + n_2}\right)^2$$
(2.53)

Concretely, in the case of the AWG, this physical phenomenon happens at the boundary between the FPR and AWs, where the light traveling from the *Si* media of the FPR undergoes reflection. Indeed, while some of the light is caught by the tapers, the other part is at normal incidence with the SiO_2 regions located between the arrayed waveguide. The large index difference induces a large reflection although the area are quite reduced in term of dimensions. In other words, there is an impedance mismatch between the 2 media. A solution to solve this problem was previously explained and consist in "impedance matching" by introducing etching in the slab and creating an intermediate area with refractive index "n_mid" such that $n_{SiO_2} \leq n_{mid} \leq n_{Si}$.

Chapter 3

Numerical methods for the fields computation

The preceding chapter was dealing with the light propagation properties of the AWG together with the physical and mathematical reasons behind the choice of our device configuration for the interface FPR/AWs which is the high loss and scattering portion of the device. Nevertheless, to simulate those sensitive sections, other ways than the simple Fourier optics formalism must be used to accurately represent the behavior of light. This is mainly due to the uncommon geometry and the high refractive index difference involving the presence of diffraction, backward reflections and power subject to be transmitted to undesirable modes. Hence, knowing the special features of our interface geometry, and the need for optimization on the parameters determining the final shape. Other, more accurate, simulations methods involving numerical methods will be used to determine the fields, and thus the figure of merit linked to the optimization process, i.e the overlap integral between the light coupled to the waveguide and the fundamental mode of the single mode waveguides. This sections covers the more useful ones, used in our simulations.

3.1   Basics

As opposed to analytical approximations using a modified version of mathematical formulations of the physical quantities, numerical analysis deals with algorithms which use numerical approximation for the purpose of mathematical analysis [46]. While those existed before the 20th century, it is from the 1950s along with the outbreak of computing power, that much more models requiring heavy computation became realistic [47]. The principle is to simulate the real behaviour of the physical quantities but with an error defined with a certain order of approximation. In our case, the physical quantities to simulate are optical fields. Like every electromagnetic phenomena, their propagation is governed by Maxwell's equations.

$$\nabla \cdot \mathbf{B} = 0,$$

$$\nabla \cdot \mathbf{D} = \rho,$$

$$\frac{\partial \mathbf{B}}{\partial t} + \nabla \times \mathbf{E} = 0,$$

$$\frac{\partial \mathbf{D}}{\partial t} - \nabla \times \mathbf{H} = \mathbf{J}.$$

$$(3.1)$$

The corresponding flux densities are

$$\mathbf{D} = \varepsilon_{\mathbf{r}} \mathbf{E} + \mathbf{P}$$

$$\mathbf{B} = \mu_{\mathbf{r}} \mathbf{H} + \mathbf{M}.$$

$$(3.2)$$

In equations 3.1 and 3.2, $\mathbf{E}$ and $\mathbf{H}$, are the electric and magnetic field vectors, respectively $\mathbf{D}$ and $\mathbf{B}$ are the electric flux density and the magnetic flux density corresponding and finally $\mathbf{P}$ and $\mathbf{M}$ are called the electric and magnetic polarization, respectively. The various other symbols are ρ the density of charges, $\mathbf{J}$ the current in the material, ε_0 the vacuum permittivity, μ_0 the vacuum permeability, $\varepsilon(\mathbf{r})$ the relative permittivity $\mu(\mathbf{r})$ the relative permeability. The last two terms depend on the position vector $\mathbf{r}$ in the material. Several observations can be made directly given we are working with *Si* and *SiO$_2$* structure which have no flowing current

nor isolated charge. Also silicon and silica are non magnetic material and finally non-linearity
and dispersion are not considered. Therefore

- $\rho = 0$, density of charge is nil

- $\mathbf{J} = \mathbf{0}$, current does not propagate

- $\mathbf{M} = \mathbf{0}$, no induced magnetic polarization

- $\mathbf{P} = \mathbf{0}$, no induced electric polarization.

3.2 Eigenmode calculation

Given a particular optical medium, where light propagates, an efficient and accurate im-
plementation of the calculation of eigenmodes in the structure is essential. Typically, for
solving field propagation in waveguides described by partial differential equations (PDEs)
resulting from modified form of the Maxwell's equations and giving a particular boundary
value problem one would like to find the solution of the propagating field in the structure.
Below, a quick overview of the numerical method will be carried.

3.2.1 Solving the wave equation and the boundary value problem

Let's consider the wave equation 3.3 obtained from Maxwell's curl equation from 3.1 in an
arbitrary, anisotropic, lossy media [48]. The conditions for those medium were listed above.

$$\nabla \times \left(\frac{1}{\bar{s}} \cdot (\nabla \times \mathbf{E}) \right) - k_0^2 \bar{\varepsilon}_r \mathbf{E} = 0 \tag{3.3}$$

With $\bar{s}$ and ε_r, 2 tensors for coordinate stretching and dielectric material. This equation must
fill up the condition

$$\hat{n} \times \mathbf{E} = 0 \tag{3.4}$$

at its domain boundaries, meaning that the field vanishes at the edges of the concerned domain. $\bar{s}$ takes the value of the identity tensor inside the propagation domain while outside of it, in the boundary layer it is given by equation 3.5 [48].

$$\bar{s} = \left(\frac{s_y s_z}{s_x}\right)\hat{x}\hat{x} + \left(\frac{s_x s_z}{s_y}\right)\hat{y}\hat{y} + \left(\frac{s_x s_y}{s_z}\right)\hat{z}\hat{z}$$

$$s_{\alpha=x,y,z} = 1 - j\left(\frac{\alpha - L}{L}\right)\delta_{\max} \tag{3.5}$$

With $\delta_{\max}$ the loss tangent, α the distance from the domain borders, and the paramters L the layer's thickness. The region, as defined above, is called the perfectly matched layer (PML) [49,50]. It guarantees small reflections at material boundaries, i.e. zone with refractive index differences such as *Si* core and *SiO$_2$* cladding. The matching with the rest of the domain is done by setting $\bar{\varepsilon}_2 = \varepsilon_1 \bar{s}$.

At this point, instead of solving for the equation directly 3.3, we solve for a modified version being the double spatial integral on the domain of interest. And then, the Anzatz using propagating field in z but defined only along x and y, $E(x,y,z) = E(x,y)\exp(-j\beta z)$ is used for both the physical modes and the leaky ones [51].

$$F(\mathbf{E}) = \iint_A \left[(\nabla \times \mathbf{E})^* \cdot \frac{1}{\bar{s}} \cdot (\nabla \times \mathbf{E}) - k_0^2 \mathbf{E}^* \cdot \bar{\varepsilon} \cdot \mathbf{E} \right] dA \tag{3.6}$$

3.2.2 FEM

At this moment the Finite Element Method (FEM) come into play. It has shown its powerful use in several electromagnetic fields solving problems [52]. Regarding the problem described by equation 3.6, the FEM is useful because instead of trying to find the basis mode functions for a large domain (the entire domain) with a complex analytical formula which is not easily solvable, it subdivides the domain into a collection of particularly shaped elements usually

triangular. This method is called meshing. It enables to find local and easier basis, which are set to disappear outside the elements. The solution for the final propagating field in the structure is a summation of all the solutions obtained for each particular elements. Nowadays, developed with complex Hybrid Edge/Node Elements it allows a very good way of providing physical modes solutions in Si waveguides.

The domain is discretized and special meshing described in [53, 54] is used. The transverse and longitudinal components are written in new basis form. Such that the transverse components take the form of $\mathbf{E}_T(x, y)e^{-j\beta z} = \sum_{i=1}^n \mathbf{N}_i E_{Ti} = \sum_{i=1}^n \{U\hat{x} + V\hat{y}\}E_{Ti}$ with E_{Ti} the field values at the element edges. And the longitudinal components the form of $E_z(x, y)e^{-j\beta z} = \sum_{i=1}^n N_i E_{zi}$ with E_{zi} the field at each node. The basis dimension n, is determined by the shape of the element used while meshing and the order of the interpolation. And finally, by minimizing equation 3.6 on each element, individual eigenvector basis are obtained as the field components at the borders and the nodes of the elements. The global solution is the sum of all of those.

3.3 FDTD

Finite-difference time-domain (or FDTD) is a method directly derived from Maxwell's curl equations. It is not an approximation and its use is not restricted to some condition. It is one of the most famous numerical method for solving for fields in mediums, even in the case of complex geometries with quickly varying envelope or backward reflections, something that cannot be done by some other famous simulation methods such as the BPM [55], which suppose a slowly varying envelope [56]. This is mainly the reason why it was chosen for the computation of the field across the irregular interface domain.

Let's first introduce how FDTD is developed. Considering the Cartesian plane, the Maxwell's curl equation, which are the 2 last in equations 3.1, give a set of 6 equations where

temporal evolution of the field **E** is directly computed from the spatial derivatives of **H**, and conversely. For example, the temporal evolution of components **H$_x$** and **E$_z$** are

$$
\begin{aligned}
\frac{\partial H_x}{\partial t} &= \frac{1}{\mu}\left(\frac{\partial E_y}{\partial z} - \frac{\partial E_z}{\partial y}\right), \\
\frac{\partial E_z}{\partial t} &= \frac{1}{\varepsilon}\left(\frac{\partial H_y}{\partial x} - \frac{\partial H_x}{\partial y}\right).
\end{aligned}
\tag{3.7}
$$

The other components are obtained analogically by rotating the x, y and z. Finite differences are then used to discretize the spatial and temporal dimensions. In space, the fields are computed on a Yee cell, a 3D element having a cuboid or cubic shape as observed on figure 3.1 [57]. Δ_x, Δ_y, Δ_z are the discretization dimensions on each side and can take different values.
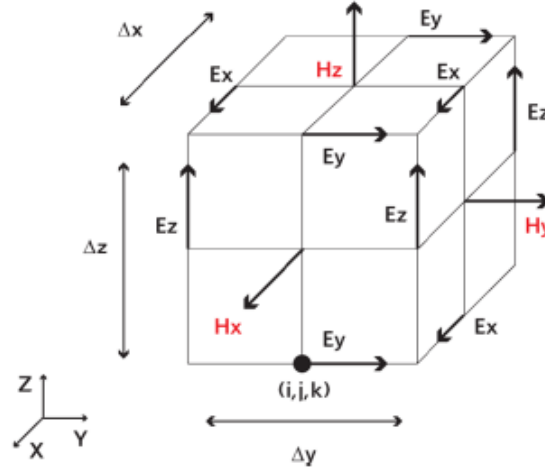
Figure (3.1): *Yee cell showing the spatial positions where the fields components are computed. The electric field components are located at the middle of the edges while the magnetic field components at the center of the faces. Δ_x, Δ_y, Δ_z are the dimensions of the grid on each side. Permission for the use of the figure is granted through the license agreement: Synopsys, Inc., Optical Solutions Group, RSoft FullWave User Guide, page 10, Figure 2.1, 2018.12*

A similar method is used temporally. Time is also divided into steps of duration Δt. Thus, the E field components are computed at times $t = n\Delta t$ and the H components at times $t = (n+1/2)\Delta t$ with n the counter for steps.

In brief, as explained, the FDTD method result in both a spatial and temporal discretization using central differences. It is an iterative "leapfrog" algorithm for which each next value for both **E** and **H** are computed using their previous value of the field to which is added the derivative curl terms of the other field, weighted by the time step Δt. The x components are given by equation 3.8 [58].

$$
\begin{aligned}
H^{n+1/2}_{x(i,j,k)} &= H^{n-1/2}_{x(i,j,k)} + \frac{\Delta t}{\mu \Delta z} \left(E^n_{y(i,j,k)} - E^n_{y(i,j,k-1)} \right) - \frac{\Delta t}{\mu \Delta y} \left(E^n_{z(i,j,k)} - E^n_{z(i,j-1,k)} \right) \\
E^{n+1}_{x(i,j,k)} &= E^n_{x(i,j,k)} + \frac{\Delta t}{\varepsilon \Delta y} \left(H^{n+1/2}_{z(i,j+1,k)} - H^{n+1/2}_{z(i,j,k)} \right) - \frac{\Delta t}{\varepsilon \Delta z} \left(H^{n+1/2}_{y(i,j,k+1)} - H^{n+1/2}_{y(i,j,k)} \right)
\end{aligned}
\tag{3.8}
$$

Last but not least, consideration when setting up the implementation of each simulation is a crucial point. The main criteria are :

- the initial excitation to be introduced, both for the temporal component of the field $g(t)$ and the spatial component $f(\mathbf{r})$

- the boundary condition at the edge of the domain usually PML [49] or periodic (for periodic structures)

- the spatial grid needs to be below a 10th of λ so as to solve correctly for it

- convergence criteria, usually automatic

- the reduction of the domain size to simulate to the more sensitive structure, keeping a dense grid and tricks to simplify the layout because the 3D computations are extremely heavy.

Chapter 4

Simulation : Methods, Results and Discussion

The previous chapter were dealing with the identification of the AWGs use in networks, the explanation of its operation characteristics, the choice of the area and elements to modify for the purpose of improving the device characteristics along with the useful numerical methods for achieving this goal. In this chapter, the simulations regarding this study are covered. As we are dealing with optical circuits in general, the AWG needs to be developed for operating in the C-band ranging from 1530 nm to 1565 nm where its attenuation is minimum [59]. The center wavelength of this band $\lambda_0 = 1.55 \mu m$ is always focused at the center of the output waveguide plane. The final goal of the project is to show the characteristics of the novel structure input in the layout and quantify its efficiency (i.e. how much it improves the transmission characteristics) at first locally and then on the overall AWG itself. In parallel, the values for the parameters resulting from design constraints imposed by high-level requirements characteristics are computed.

4.1   Method and set up

4.1.1   Metrics, references and types of data

The first big and perhaps most important part of the simulations will be to correctly model the light adiabatic transformation taking place at the boundary between the FPR and the AWs and from there, optimize geometrical parameters in order to have a maximum of power converted into the ideal signal. By ideal signals, it is signified the fundamentals modes of the structures, some other modes of interest or a predefined signal. To measure this conversion, there are various metrics to be used. At first, the overlap integral between the propagating field $\phi_p(t)$ at the position defined by the measurement monitor and the test field ϕ_0 (the field one whishes to obtain). Figure 4.1 shows a simple linear waveguide simulation with the launched site and monitor of measurement side. In all the layout take from FullWave CAD, the monitors are green and used to record the data.
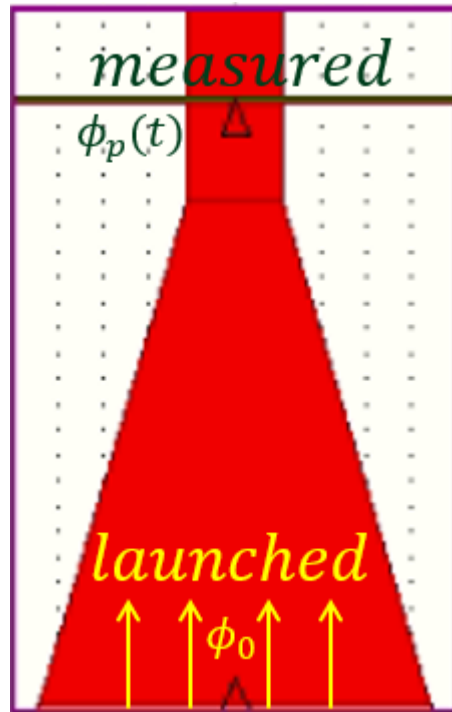
Figure (4.1): *Arbitrary 2D linear taper configuration to show the references used for launching and measuring in the simulation program*

More precisely, the overlap integral will be computed by translating the test field to the center location of the monitor and rotating it so that it lies in the X'Y' plane of the local monitor coordinates. It is similar, if not equal, to the coupling coefficient given by 4.1 in the wavefront matching method (WMM) between the arbitrary propagating $\mathbf{E}$ incident electric field and $\mathbf{H}_m$, the magnetic fields of the desired mode profile. In this case, P_{src} and P_m are the total input source power to the system and the power carried in the desired mode.

$$\eta = \frac{1}{4P_m P_{\text{src}}} \left| \iint_A d\mathbf{A} \cdot \mathbf{E} \times \mathbf{H}_m^* \right|^2 \tag{4.1}$$

The second metric that can me used, in the case of no prior idea about the special mode to reach or just to compute the total ratio between the power transmitted (not in just in a particular mode with the overlap) compare to what is sent at the input is to record the total power flow crossing the measurement site S(t) such that

$$S(t) = \frac{1}{S_0} \text{Re} \left[\int_A [\mathbf{E}(\mathbf{r},t) \times \mathbf{H}^*(\mathbf{r},t)] \cdot d\mathbf{A}. \tag{4.2}$$

In equation 4.2, $\mathbf{E}$ and $\mathbf{H}$ are the electric and magnetic fields and S_0 is the launch power. The integral is evaluated over an area A. The definition of A depends on the monitor length in our case the length of all monitors along z is always 0 and launched field are always launched in z direction. Typically we just record and simulate the power flows in the direction of propagation. The last point about measurements, but this time not being a metric for optimization purposes but for showing the physical properties and transformation of light in one part of the device, is to record the spatial output of some field or of the power. These data can thus be used to simulate other part of the device where FDTD is or is not employed.

4.1.2   Geometrical optimization process

Back to the interface layout problem, the simulations will help to choose the most suitable design in terms of combination of tapers and etching and the geometrical parameters values. Typically, the choice can be made for the taper to be either linear or parabolic as explained in chapter 2. Those two configurations are presented on figure 4.2 along with their paramaters for the length L and parabola pitch d.
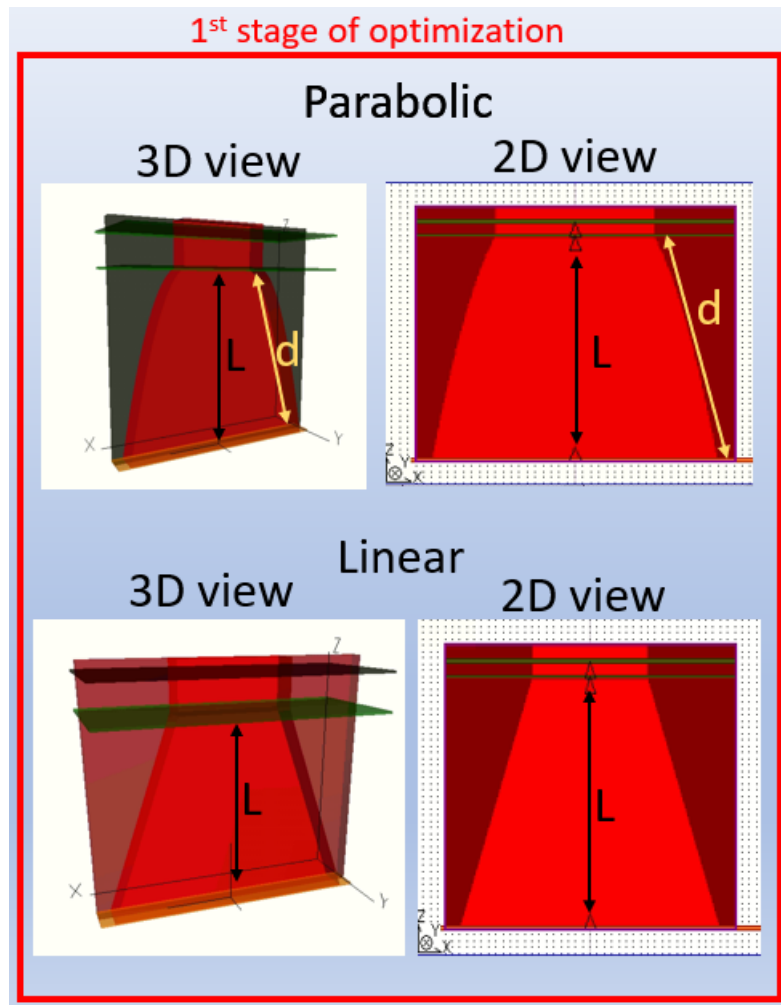

Figure (4.2): *The first stage is optimized using these 2 structures. on the top the parabolic shape taper, on the bottom the linear shape taper. Left side represent the 3D view, right side represent the 2D view. In green, the monitor where the overlap integral (power transmitted to the fundamental mode) are recorded.*

Then, the arrangement of the taper and slab can be selected between two structures as well. Either by a "combined" structure where the taper and etching rib are two-in-one, as seen on the bottom of figure 4.3. This actually means that the half-etching and then full-etching are made along the taper's length. Here, attention is made to the reader that the "rib waveguide" is forced to have its lower slab element width reduced gradually in the z direction as the etching area progresses until the layout finally reaches the waveguide grating composed by single mode Si waveguides. The other possible arrangement, allowing more degrees of freedom, is to use a 2 stage design using at first the taper and then only the rib waveguide, as exhibited on the top of figure 4.3. As a result of combining the two stages in one, one variable (degree of freedom) is lost for the optimized structure. Table 4.1 summarizes the two step process.

Technique	Alternatives		Metric
Tapers	Linear	Parabolic	O
Arrangement	Taper + Rib : combined	Taper then Rib : 2 stages	O and P_{out}

Table (4.1): *Interface shape and dimension optimization elements, arrangement and metrics (O : overlap, P : power)*
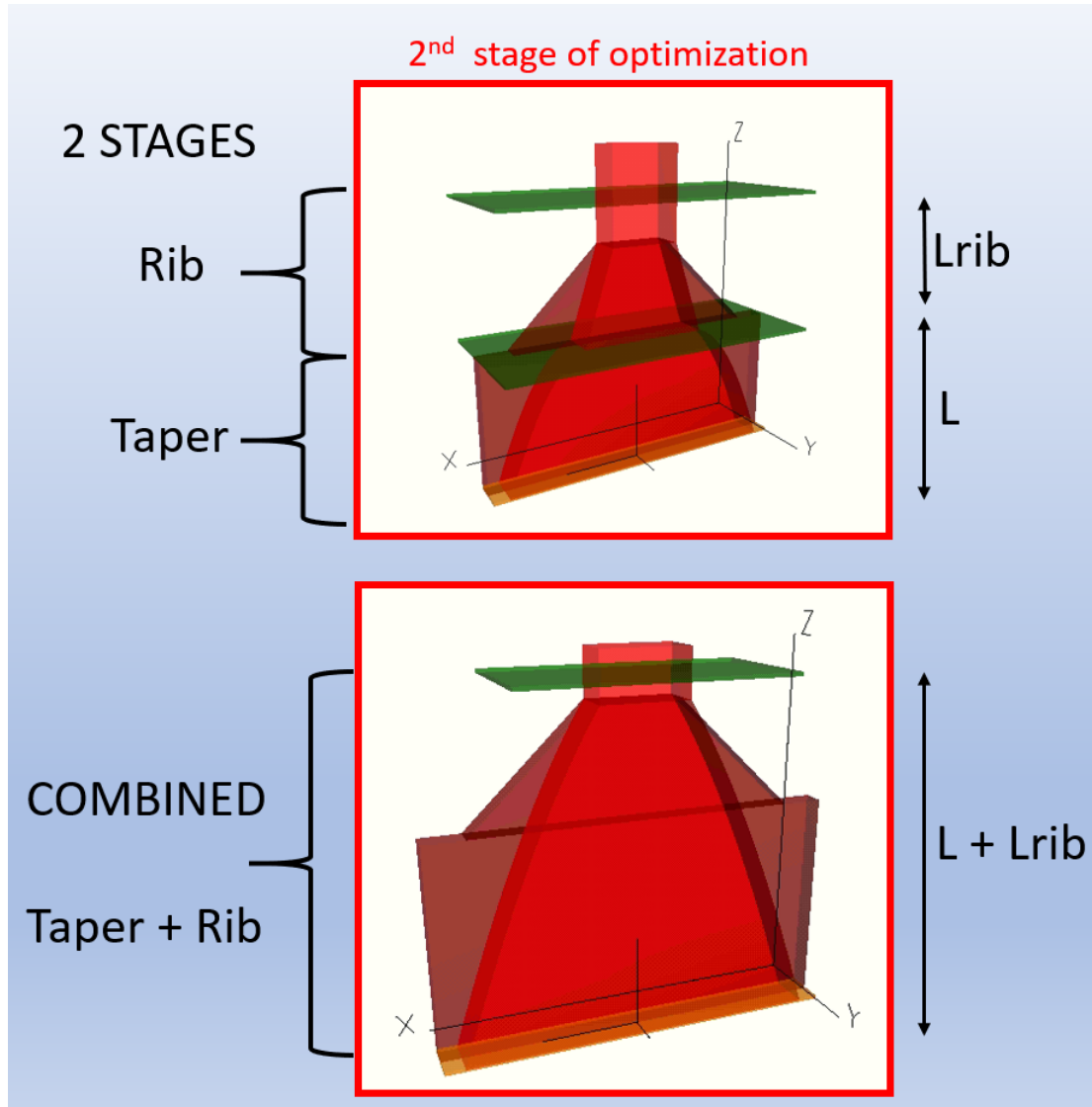
Figure (4.3): *3 dimensional view of the two possible arrangement for one unit of the FPR/AWG interface. The first one on the top uses a parabolic taper then independently a rib waveguide. The bottom one instead combine both at the same time. In green, the monitor where both the overlap integral (power transmitted to the fundamental mode) and normalized the power are recorded. Based on the values, the choices of best design is carried out.*

Finally, because the light is coupled from the slab into the single mode waveguides of the AWs. So as to obtain the initially optimized structure, the overlap integral metric between the launched field in one unit and the fundamental mode of those single mode waveguide is chosen. The geometrical parameters of each constitutive part of the structures are varied and

global optimum is approached by finding the maximum overlap values for those combined set of paramter values. The symbols for the parameters that can be varied as well as their physical meanings are compiled in table 4.2. Also, a global interface layout with all the geometrical parameters represented spatially is displayed on figure 4.4. It has to be noted that the *Gap* between waveguides, the waveguide input width *Win* as well as the output width *Wo* are fixed all along the process. Also, as a remark, while transmission is calculated by inputting light in the central waveguide and measuring the response in the central output waveguide, by analogy the crosstalk is obtained by measuring the response by adjacent waveguide monitors while coupling light in the central input waveguides.

Parameter symbol	physical meaning
L	length of taper
Lrib	length of rib structure
Wmid	width of rib waveguide
d	pitch of the parabolic taper

**Table (4.2):** *Parameters varied in the etching optimization*
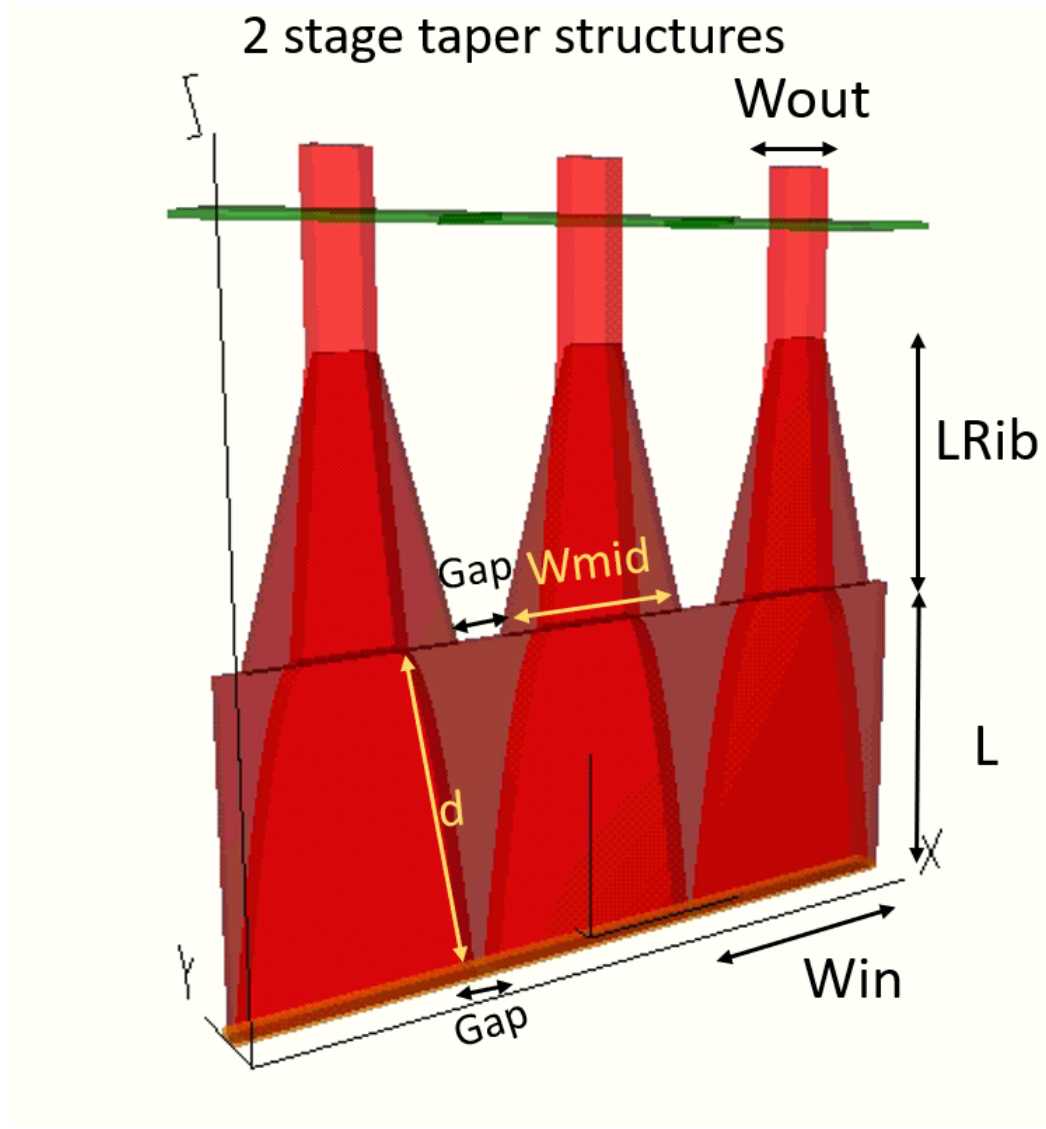
Figure (4.4): *The global interface structure with the various parameters represented spatially. It is to be noted that the gap between waveguides Gap, the taper width at the input Win, and the taper width at the output Wo are fixed. The overlap integral coupling to the fundamental mode of the arrayed waveguide is recorded by the monitors in green compared to a unit power value sent in an individual taper.*

The last interface simulation for improvement of the transmission profile which has been carried out is the slab etching optimization. A vertical cut of the layout representing the etched area can be seen on figure 4.5 while figure 4.6 display an artistic view of the interface FPR/AWs. The etched area are shown in light blue and the 3 parameters being optimized by a
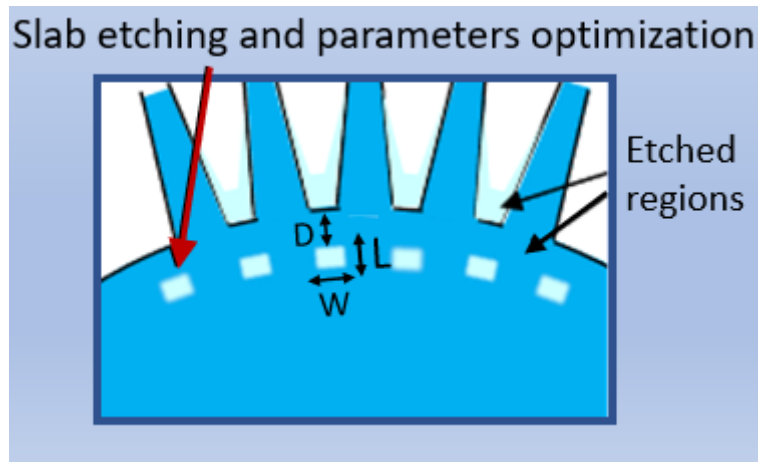
gradient techniques based on the data obtained from the simulations. The idea behind this logic comes from that by introducing etching in the slab, it could be possible to actively modify the refractive index distribution at this interface. Therefore, by tuning the geometries of the etchings we could possibly tune the light transmission at the interface. Three parameters are then used to do so : the etching distance relative to the tapers' interface *detch*, the etching area length in z-direction *letch*, the etching area width in x-direction*wetch*. Table 4.3 summarize the parameters and the physical meaning those bear.

Parameter symbol	physical meaning
detch	etching distance relative to the slab interface
letch	length in z-direction of the etching area
wetch	width in x-direction of the etching area

Table (4.3): *Parameters varied in the etching optimization*
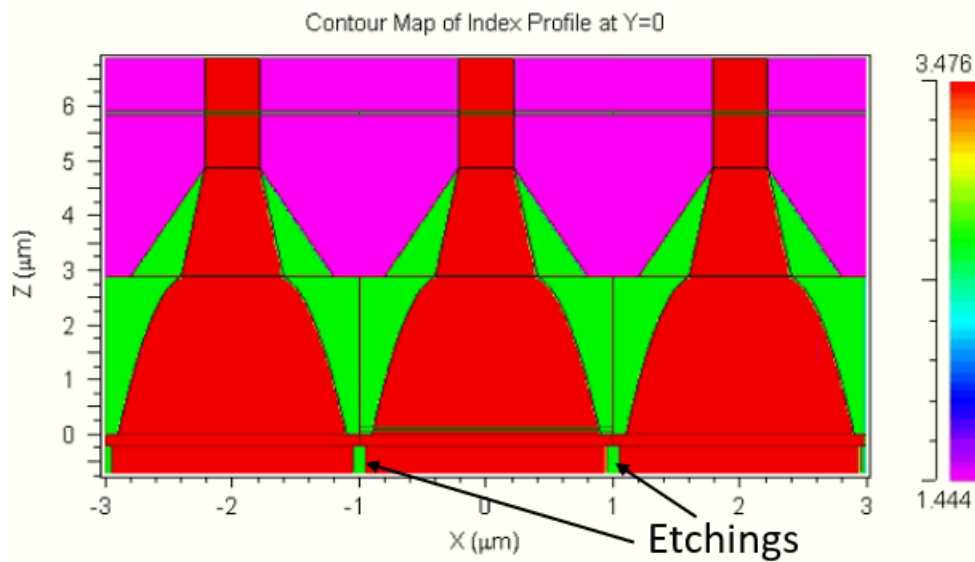
Figure (4.5): *Refractive index profile vertical cut of the slab etching layout used for the simulation.*

Figure (4.6): *Artistic view of the interface where the 3 parameters D, L and W (detch, letch, wetch) being optimized by a gradient techniques based on the data obtained from the simulations are displayed*

To conclude this part, evaluation of the improvement brought by our devices can be quickly performed after the end of each optimization process. In other words, after the interface geometrical optimization and after the etching area optimization. The flow of the the optimization/evaluation process is organized in table 4.4.

Successive Order	Geometrical Optimization	Parameters
1	Interface Optimization	*L*, *Lrib*, *Wmid*, *s*
2	Comparison	linear structure
3	Etching in slab	*detch*, *letch*, *wetch*
4	Comparison	linear structure

Table (4.4): *Successive geometrical optimizations and improvement evaluations of the FPR/AW interface*

4.1.3 Crosstalk and link with overlap integral

The previous 2 stage optimization process as described above only optimize the transmittance by maximizing the overlap integral at the output part of the structure. Regarding the optimization of the AWGs, one can decide to also optimize the crosstalk but this will be only done by a trade-off on the transmittance, i.e. if crosstalk optimization is performed than the optimum values of the parameters will change and it will worsen the transmittance. This study instead choose to mainly focus on transmittance optimization. However, the crosstalk wasn't ignored in the computations. Figure 4.7 displays how the crosstalk can be computed on an arbitrary interface by measuring the overlap integral in the adjacent waveguides while power at a given wavelength is launched in the central waveguide.
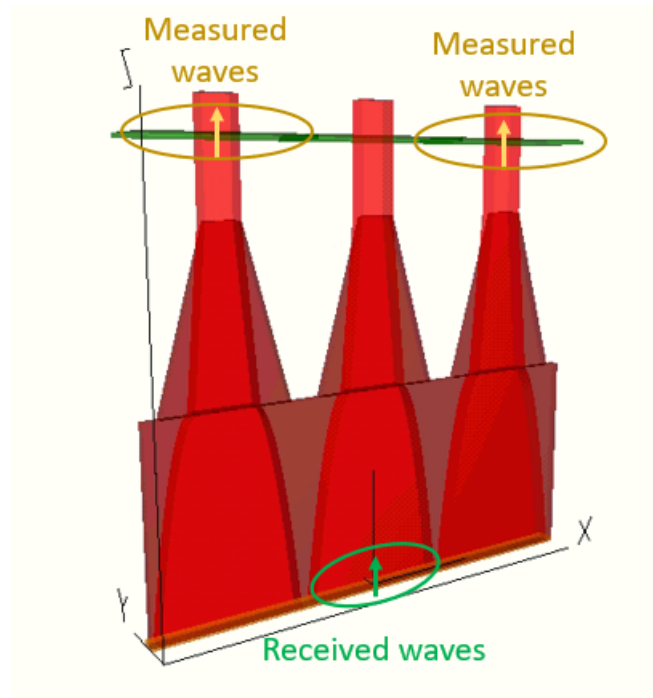

Figure (4.7): *Arbitrary and simplified schematic showing how the crosstalk between adjacent channels is measured. An input wave is received by the middle channel, at the location circle in green. While the overlap integral is computed at the output of the adjacent channel, giving the measure of the power coupling to the fundamental modes of the adjacent channels.*

To have a full picture of the crosstalk, this method needs to be repeated for the entire spectrum of operation, what wasn't achieved. This simulation is particularly tedious and time consuming using FDTD as the complete computation of all the values of the fields in the entire device needs to be repeated many times. As a result, choice was instead made on focusing on the transmittance optimization and simpler simulations were performed with only the central wavelength of operation λ_0 relatively to the effect on its adjacent wavelength. This quick analysis only computes the crosstalk between two adjacent wavelength, giving low values. The overall crosstalk could be computed and would give higher values.

4.1.4   Overall AWG characteristics

The second simulation step concerns the overall AWG characteristics obtained through simulations. As opposed to the mathematical development of chapter 2, we are not using pure analytic equations, which need some strong hypothesis to be analytically resolvable. Also, these equations suppose an overly simplified interface. Examples of these simplifications in the mathematical models are the simplified mode profiles (Gaussian beams), not considering the transition losses (but just the coupling losses). Instead, we obtain the fundamental waveguide modes and slab modes by FEM, this also gives the effective refractive index n_{eff} of each mode. Similarly, the previously optimized interface is included at the slab/arrayed waveguide interface and 3D-FDTD is employed for obtaining more precise values for fields and power between, before and after the interface transition and thus the power drop, scattering or crosstalk resulting. However the analytic equations of chapter 2 are useful to understand the physical phenomenon or mathematical operations taking place in the devices. This is helping in setting guidelines for customized numerical methods. This concerns the fraunhofer diffraction for the slabs and arrayed waveguide phase factor as well as both of those effects on the fields at interfaces. Also the custom code reduces the computation time that other more complex algorithm would take. The all process is displayed on figure 4.8.

The new layout presented on figure 4.8 describe the all simulation process, including the technique used at each stage. Using FEM for computation of the ideal fundamental modes. Those are then used to compute the coupling efficiency. At the FPR/AWs interfaces, the new structure is introduced. As explained in chapter 3, FDTD is a better method to obtain accurate results for the fields in these regions. The delay in the waveguide will be introduced using a customized code treating the obtained data after the interface.
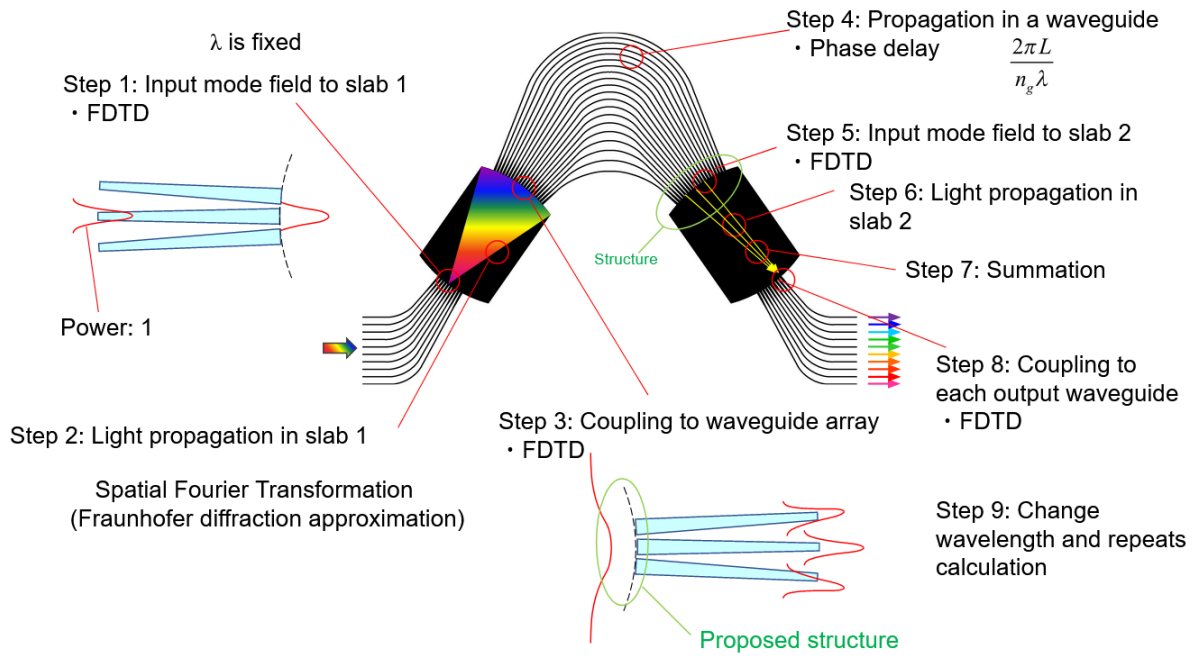
Figure (4.8): *Global view of the AWG with each successive simulation undergone by the input light ranging from step 1 to step 9. Each simulation is performed using a fixed wavelength. Those operation include diffraction, coupling to AWs, dephasing, and coupling to the second slab where the final output is a a summation of field spatially distributed along the second FPR/output waveveguide interface therefore demultiplexing the input field.*

4.2   Results and discussion

### 4.2.1   Geometrical optimization process

First stage

The first stage is just a simple taper. Therefore the number of parameters is limited. For the linear taper the only variables that can be scanned are the final width where the rib waveguide is supposed to be inserted *Wmid* and the length of the taper's first stage *L*. What is interesting is to set a few values for *Wmid* (having less impact on the loss, it is just there for accommodating the second stage) and scan on a large number of length value to obtain the profile. It means we build a 2 dimensional power profile for the linear taper. The exact same remarks apply for the parabolic taper although this time the parabola parameter *d* is additional. But this one is not totally independent from the length of the taper, as the input and output width are set constant. However, some tuning of *d* is possible. On the following graphs, the overlap integral for the centered waveguide output is represented by a blue curve. Accompanied to this curve, is the orange curve of the normalized power. Ideally, at the end of the second stage, the 2 curves should fit each other at the same time as they should reach a highest level possible. The fact that the 2 curves match each other means that all the power at the monitor in converted into fundamental modes of the arrayed waveguides, not transfered to other modes or scattered. The linear taper data are represented on figure 4.9 and 4.10. In the following figures, the overlap integral is normalized by both the input power and the power carried in the desired mode while the power is only normalized by the launch power. For all simulations unit input power was used.
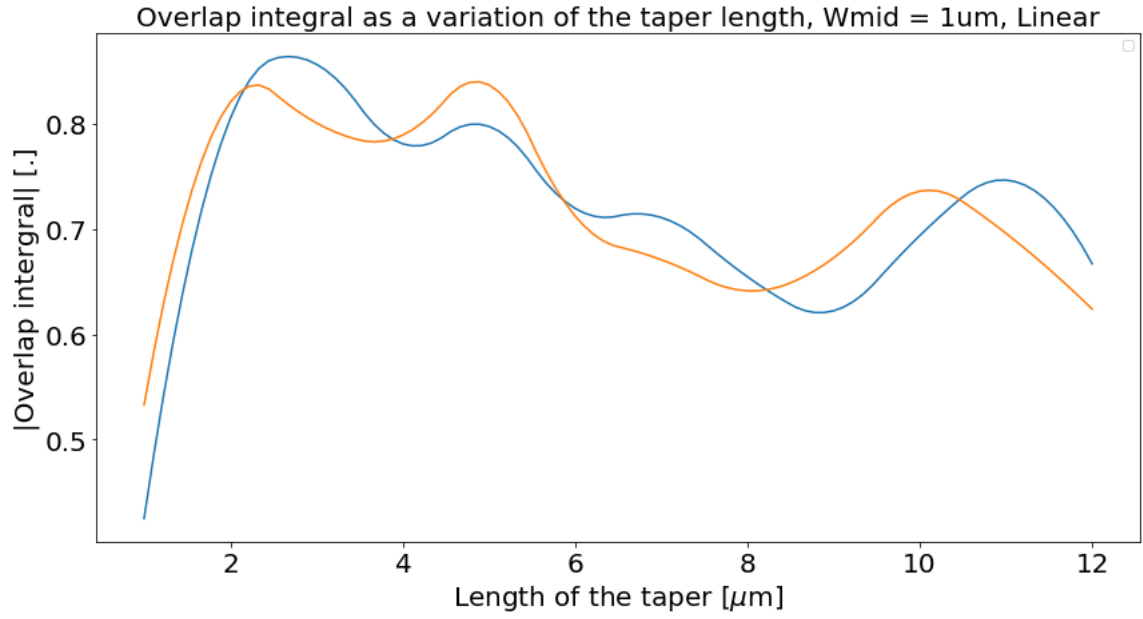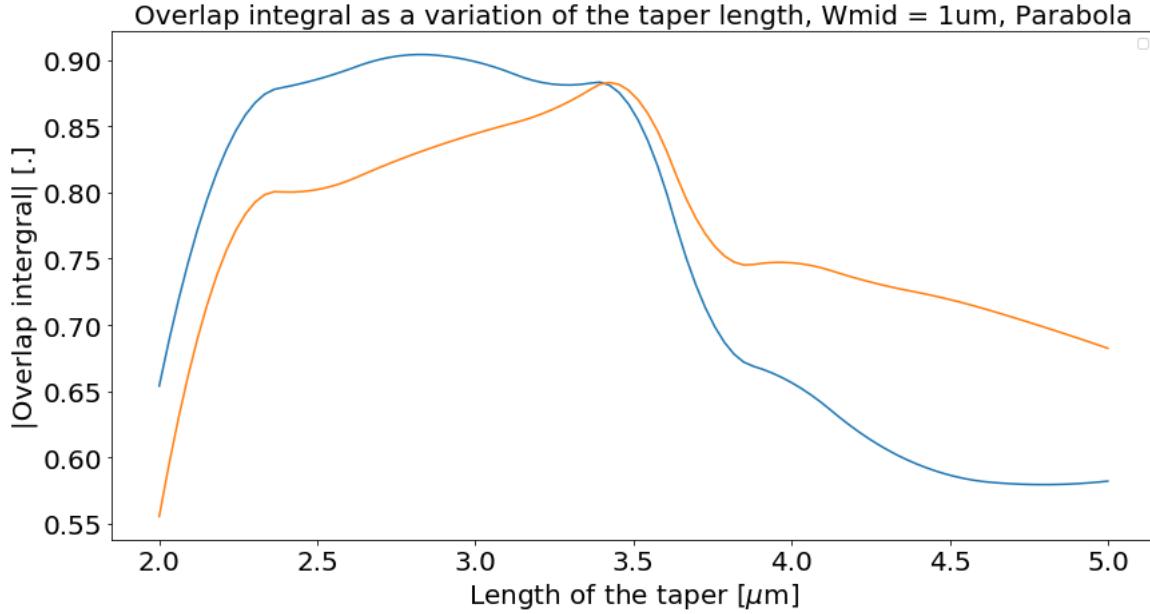
Figure (4.9): *Overlap integral with the variation of the length for a linear taper configuration with Wmid = 1um. The blue code for the normalized overlap integral, the orange code for the normalized output power.*
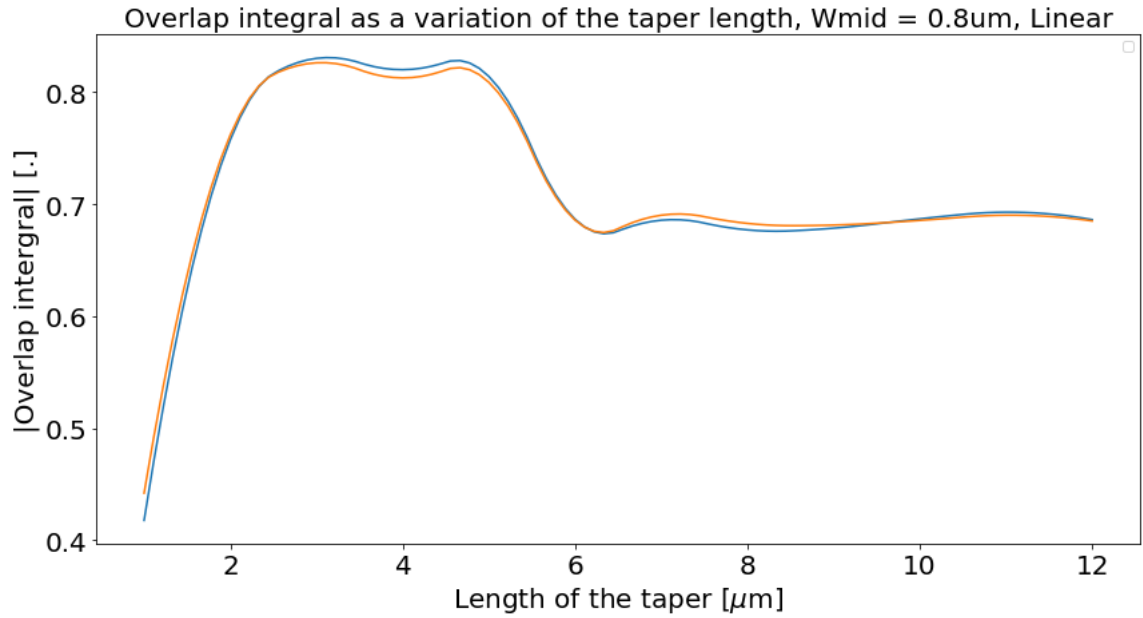
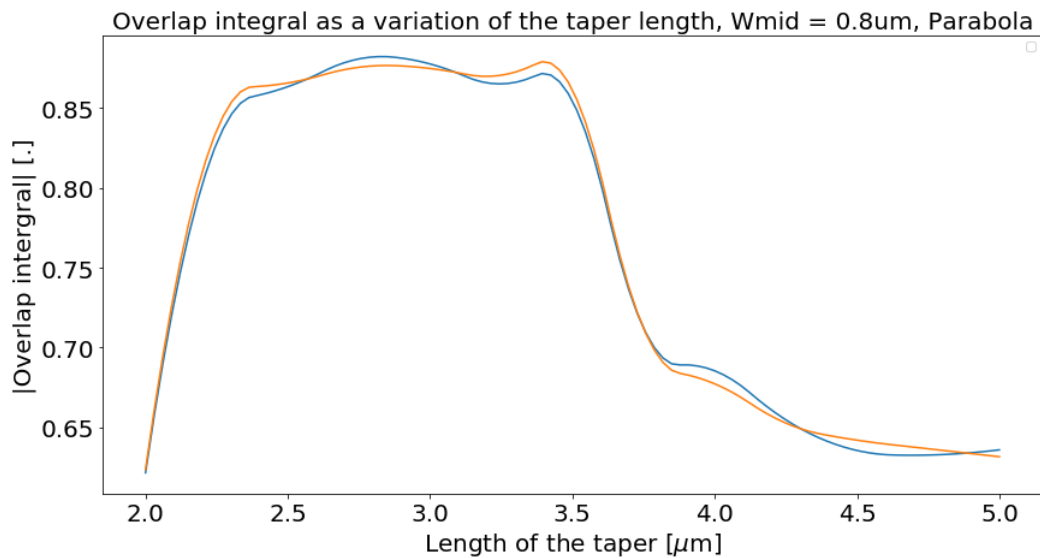**Figure (4.10):** *Overlap integral with the variation of the length for a linear taper configuration with Wmid = 0.8um. The blue code for the normalized overlap integral, the orange code for the normalized output power.*

The parabolic taper data are represented on figure 4.11 and 4.12.

Figure (4.11): *Overlap integral with the variation of the length for a paarabolic taper configuration with Wmid = 1um. The blue code for the normalized overlap integral, the orange code for the normalized output powerl*
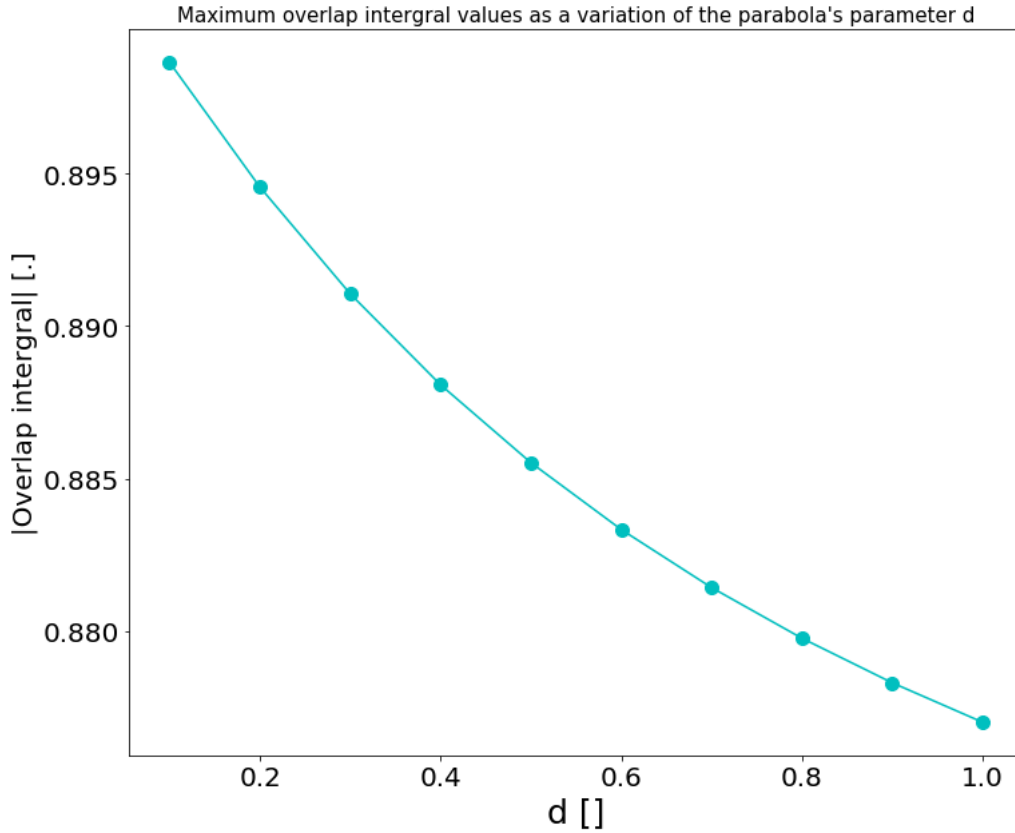

Figure (4.12): *Overlap integral with the variation of the length for a parabolic taper configuration with Wmid = 0.8um. The blue code for the normalized overlap integral, the orange code for the normalized output power*

Figure 4.13 shows that even though the value range on which the parameter *d* can be tuned for bringing improvement is limited, because after the different value converge to a unique value, it still brings important improvement to the power converted in the fundamental mode.
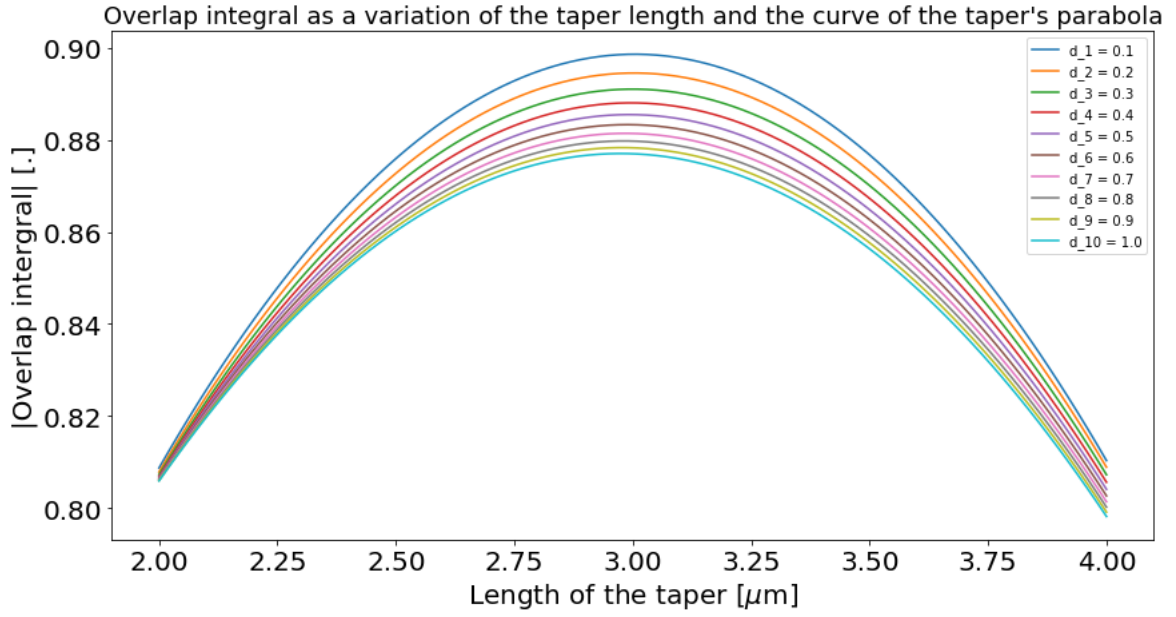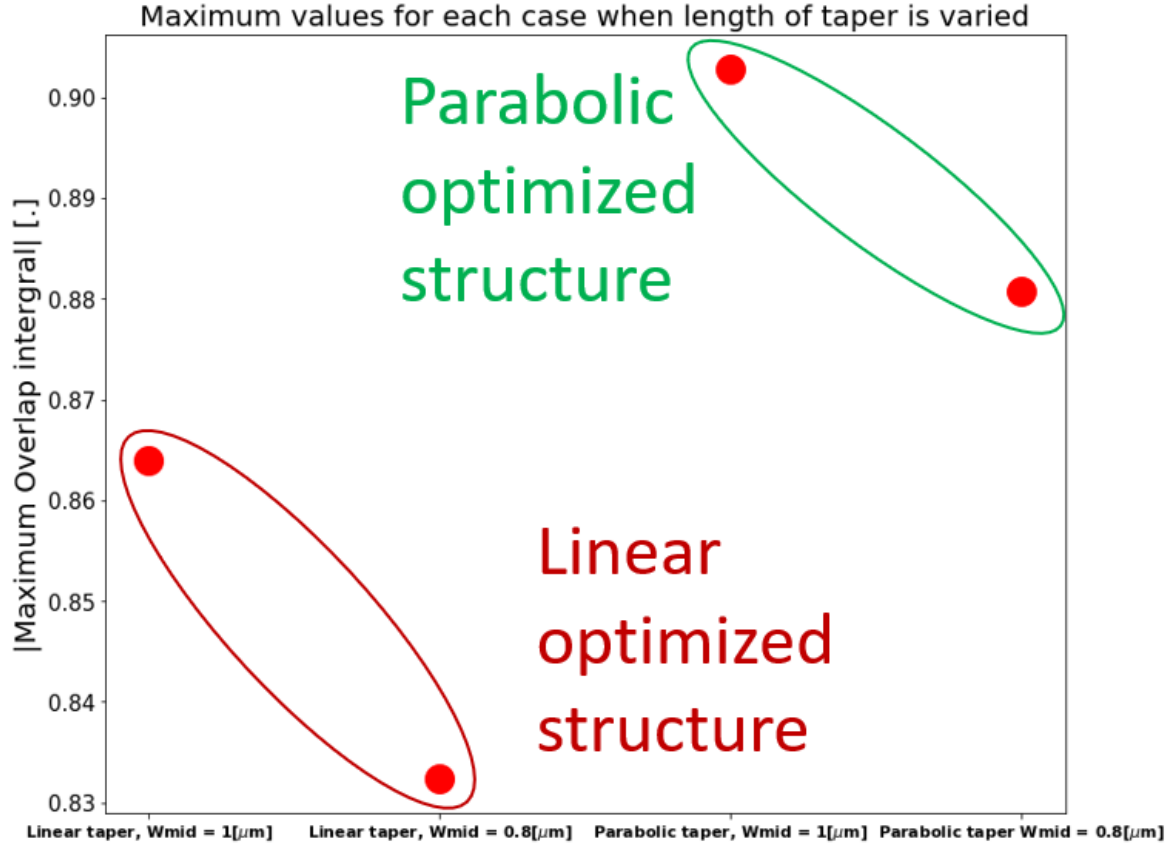

Figure (4.13): *Variation of the overlap integral as a function of both the length and the d parameter.*

Figure (4.14): *Variation of the overlap intergral with the d parameter using the optimal length and Wmid*

Quickly analyzing those graphs give us information that the power level is higher for parabola than linear tapers. And *d* should be chosen as small as possible for high transmission characteristics, as displayed by figure 4.14, where the curves increases as d decreases. The values of the overlap while all the parameters are optimized is displayed for comparison on figure 4.15. As a conclusion linear tapers are lower in performances. *Wmid* = 1 *μm* tends to have higher value of transmission but seems to cause greater differences in the two curves which is not significantly important at this stage. At the end, we want to couple to the fundamental mode of the arrayed waveguides not the fundamental mode of the *Wmid* waveguide. The beam still needs to converge what will be assured by the second stage tuning. The choice for the higher transmitted value prevails at this stage.
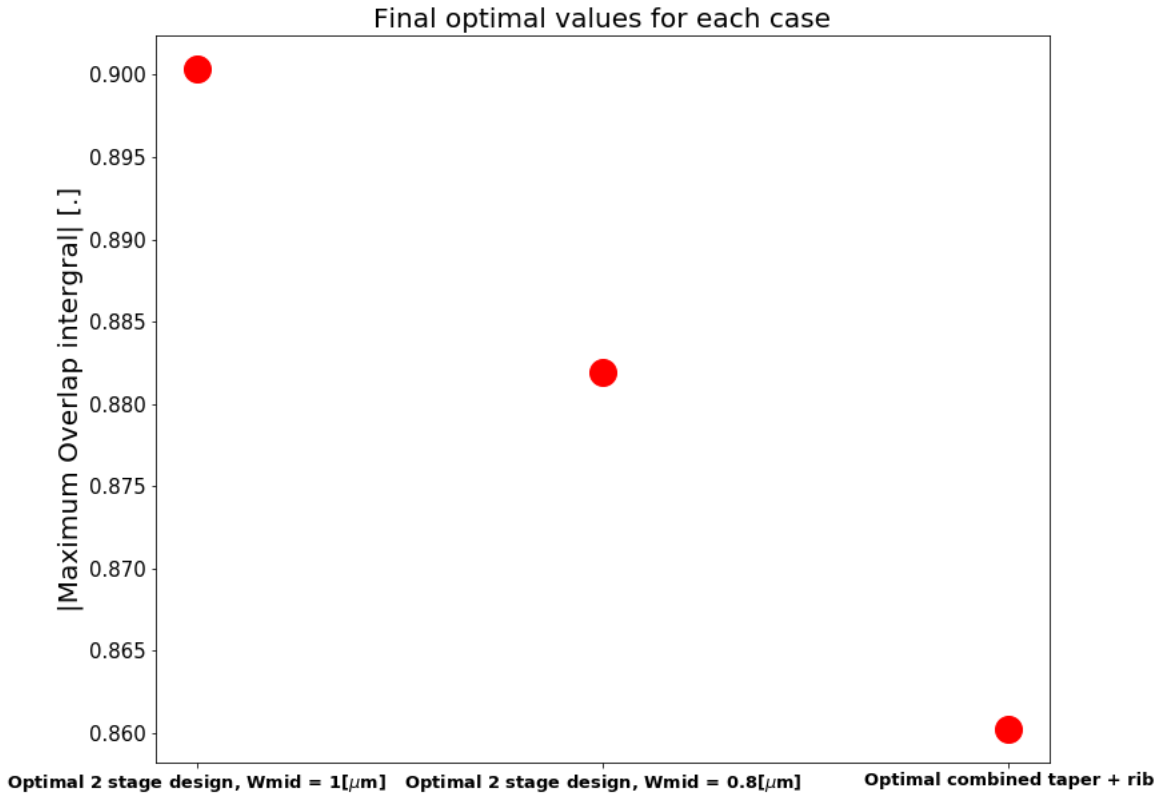
Figure (4.15): *Comparison of the overlap integral levels for both linear and parabolic structures given several values of Wmid.*

For indication this stage is therefore optimized using a parabolic taper which is the main result. Also *Wmid* = 1 μm, L = 2.8 μm and d = 0.1.

Second stage

The second stage is optimized in a similar manner than the first one. Explanation on the parameters behaviour does not subtantially change and the analysis is the same. However, this time the differences in the two curves become an important problems. The best design choice determined to improve step one are used and the length of the rib is found to be the

one giving the best output in the profile. To go to the point, the direct synthesis of the optimal
values for the 2 stage and the combined design are displayed on figure 4.16.

Figure (4.16): *Comparison of the overlap integral levels for both 2 stage structure and the
combined structure, all the parameters values being optimized.*

Clearly, the 2 stage design with *Wmid* = 1 μm, *L* = 2.8 μm, *d* = 0.1 and *Lrib* = 2 μm allows to
reach the highest transmission and coupling to the fundamental mode arrayed waveguides.

Comments

With respect to the curves aspects several comments can be made. At first, the graphs
displayed from figure 4.9 to 4.12 exhibits curves for which the values of the overlap integral
first increases and then decreases when the length of the taper is larger. This seems to be
due to the coupling which tend to increase when the taper's length increases. It means that

the light received by the central waveguide on figure 4.4 couples more to the two adjacent waveguides by its sides. Also, the point that parabolic taper gives higher transmittance than the linear taper as stated [26] [27], is confirmed by the curves shown above. Finally, given the look of the curve, an advantage that can be noticed is that the device allows to have highly efficient tapers of reduced sizes, reducing the footprint of the all AWG.

One of the possible reason why the two stages interface exhibit better characteristics is that in the optimization process there is one more parameter that can be controlled, so one more degree of freedom compare to the combined structure. So we can control both the taper part (first stage) and then adapt the rib waveguide part (2stage) successively to obtain better results.

4.2.2 Etching in the slab

This newly introduced modifications of the boundary was simulated in using the three variables : the etching distance relative to the tapers' interface *detch*, the etching area length in z-direction *letch*, the etching area width in x-direction *wetch* described earlier. Now, these etching areas parameters cannot take any range of value and their dimensions are quite limited. Those stay small in reality. This is because of what follows. First of all, these cannot be smaller than 0.2 μm because this is the fabrication limit for etching area. Also if *detch* is too big then it just does not make any effect on the boundary, i.e. too far from the interface then not tuning the light profile at this interface. This limits its values around 1-1.5 μm. *Wetch* is limited to around 1 μm because the waveguide input width *Win* is 2 μm so it cannot be bigger than half of it or the material at the interface would be predominantly SiO_2 instead of SiO_2, what is not meant to happen. The limitations on *letch* are less evident, but at the beginning, the same range of values than the others will be considered. So the range of values for those are considered to be included in $[0.2\mu m, 1\mu m]$. This news is quite important when referring to the simulation point of view. Because in the previous geometrical optimization

method the range of values were too large up to 10-20 μm in the z-direction and several μm direction in the others, a scan on all the parameter at the same time was not an options. This is because FDTD takes too much time for large dimensions and the vector of values being large there would have been too many steps in the simulations. But the point is that here, the simulation being small a 3 dimensional scan on the parameter vector is feasible. This is what was realized, we have values of the overlap over the all parameter space and choose an optimum. The FDTD final windows of one simulation, with the Ex field propagating, can be seen on figure 4.17. It is seen from this first graph that the designed interface, even including the etching, in the slab converts the mode in an adiabatic manner. Typically very good transmission characteristics are exhibited.
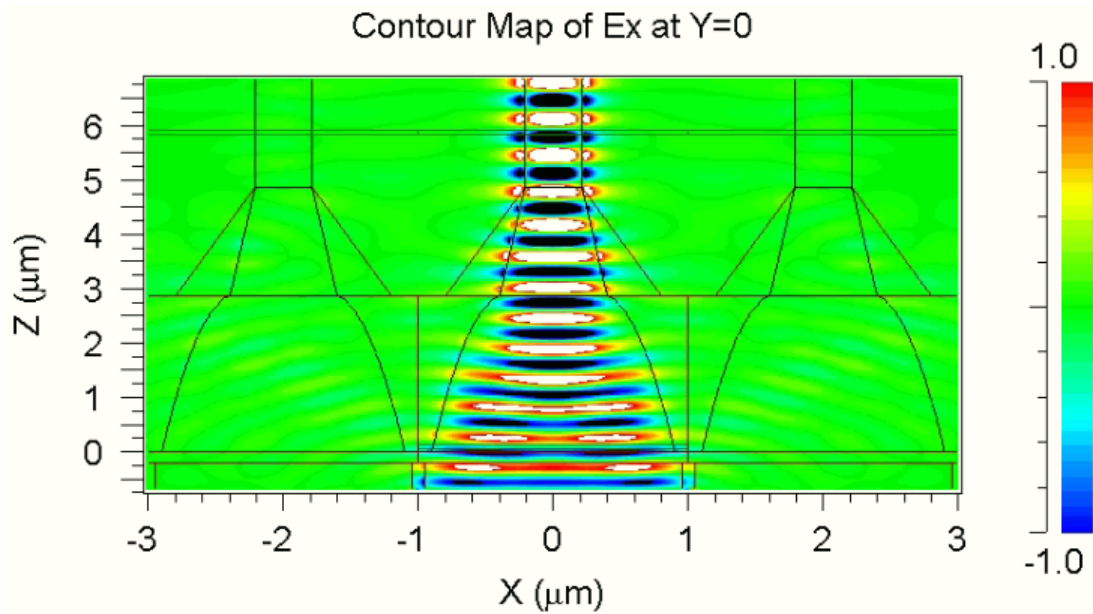

Figure (4.17): *FDTD final windows with Ex field amplitude converted from a slab mode in the FPR into a fundamental mode of the arrayed waveguide.*

This first observation is confirmed by the normalized power profile measured at the central waveguide, typically the waveguide receiving the light in the previous figure, and displayed on figure 4.18. In each dimension, only 2 values were scanned, for a quick simulation of 8 iterations giving already good outputs. This final simulation results using the optimized

devices previously developed, seem to confirm that light propagation can be tuned via etching sites in the slab and along the interface. This needs to be further investigated in the rest of the research. The parameter value giving a transmission of around 92% are *letch* = 0.4 *μm*, *detch* = 0.5 *μm* and *wetch* = 0.2 *μm*.

Intuitively, one can consider that the etching in the slab improves the transmittance because it matches better the impedance of the transition regions.
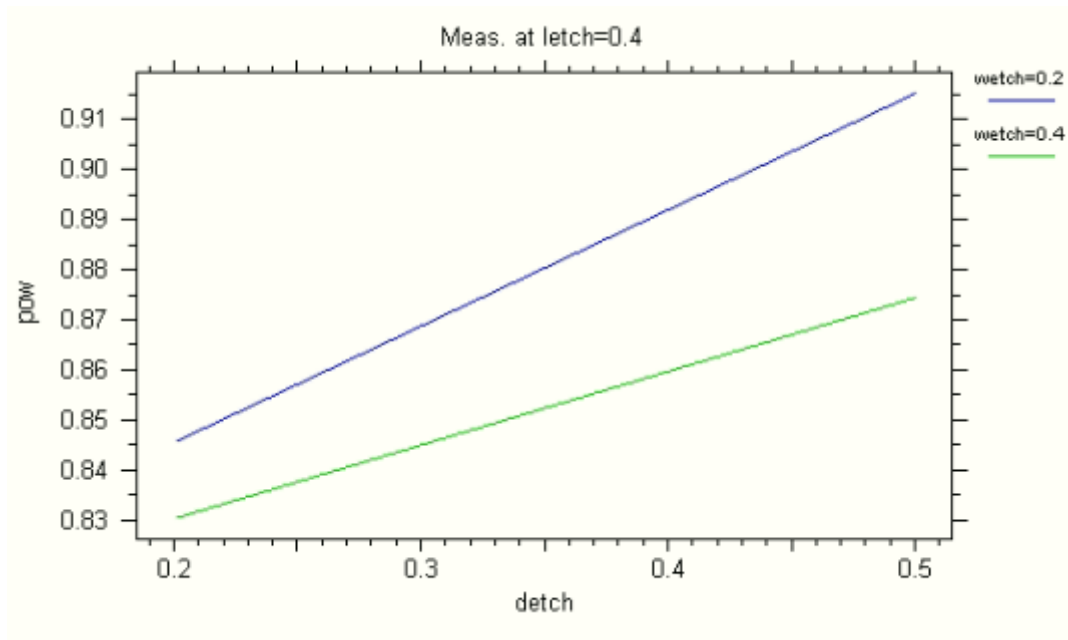
Figure (4.18): *FDTD optimal set of parameters with maximum power values for 3 dimensional scanning on the parameters. letch = 0.4 μm, detch = 0.5 μm and wetch = 0.2 μm.*

As a quick evaluation, the loss is estimated to be 0.3 dB for the central output waveguide and the crosstalk -26 dB with the simplified definition only considering two adjacent channel, as explained in section 4.1.3.

4.2.3 AWG design parameters

The AWG parameters depends on the WDM networks requirements called the high-level requirement. When some high level requirements are set up then the methodology developed

by [38] allows to compute step-by-step the AWG requirements. Ideally, Si AWG would have 32-40 OW channels. But in this case, the AWG exhibits very poor characteristics and is thus not really suitable for applications. Instead, one would prefer using 8 channels, 400 GHz channel spacing. The parameters for the AWG simulated here are available in table 4.5.

Design parameters	Value
Operational wavelength λ_0	1550 nm
Channel spacing Δ_{CH}	3.2 nm
Frequency channel spacing Δv	400 GHz
Number of channels N_{CH}	1×8
$\Delta\lambda$ (FSR)	25.6 nm
Free spectral range (FSR)	$1.5 \times 25.6 = 38.4$ nm
Focal length of slab waveguide (L_f)	88.803 μm
Number of arrayed waveguides (N)	25
Path difference of arrayed waveguides Δl	26.8998 μm
Separation between the input/output d_{wg}	2 μm
Gap between the waveguide gap	0.2 μm
Separation between the arrayed waveguides	2 μm

**Table (4.5):** *Design parameters for Si AWGs with 400 GHz channel spacing*

4.2.4 AWG characteristics

Finally, after completing the local optimization method, the last simulations required are the actual AWG characteristics. The locally designed part in not very useful if it does not take part into an operating device for which the requirements are meaningful for achieving correct light transmission. Itself included in a larger view such as the AWG are included in WDM networks to perform the multiplexing and demultiplexing operations. The precise

numerical methods will not be detailed in this work as this is clearly out of the context of the AWG. However, code and designed method will perform step by step the described actions by figure 4.8. More precisely, the data relative to the effect induced by the device on the signal from the input waveguide to the FPR1 and the AWs (arrayed waveguides) to FPR2 are obtained by 3D-FDTD, supposing a conventional linear tapered interface. The data of the transmission between the FPR1/AWs are also simulated by 3D_FDTD, this time introducing the new developed 2 stages layout. However, the diffraction pattern, the phase in the array, the sampling when entering the AWs and the reconstructed wavelength output spectrum on the output waveguide (OW) interface are numerically implemented. Eigenmode calculation described in section 3.2 is used for mode computation.

Input and first FPR

The input waveguide is a fundamental mode waveguide. The data for this mode are obtained by FEM using as dimensions of 0.43 μm for the width and an height of 0.22 μm. The FEM mesh as well as the initially computed mode can be seen on figure 4.19 and 4.20.
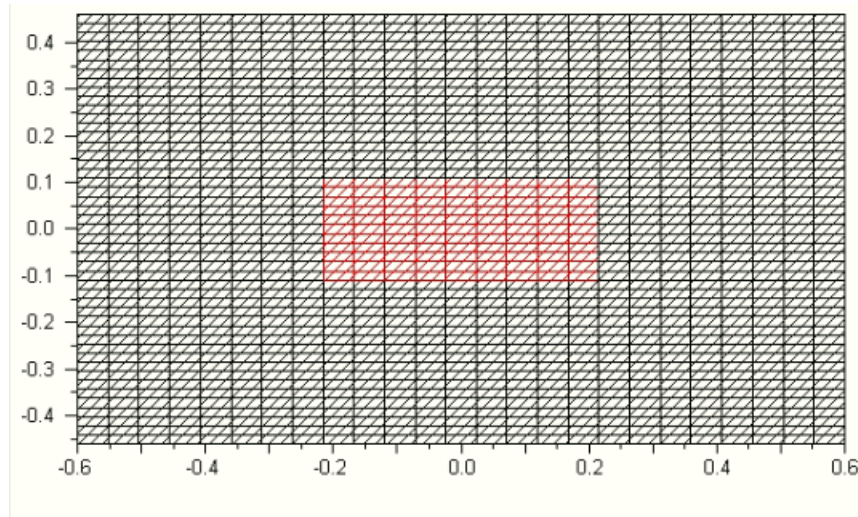

Figure (4.19): *FEM mesh solving for the single mode waveguide*
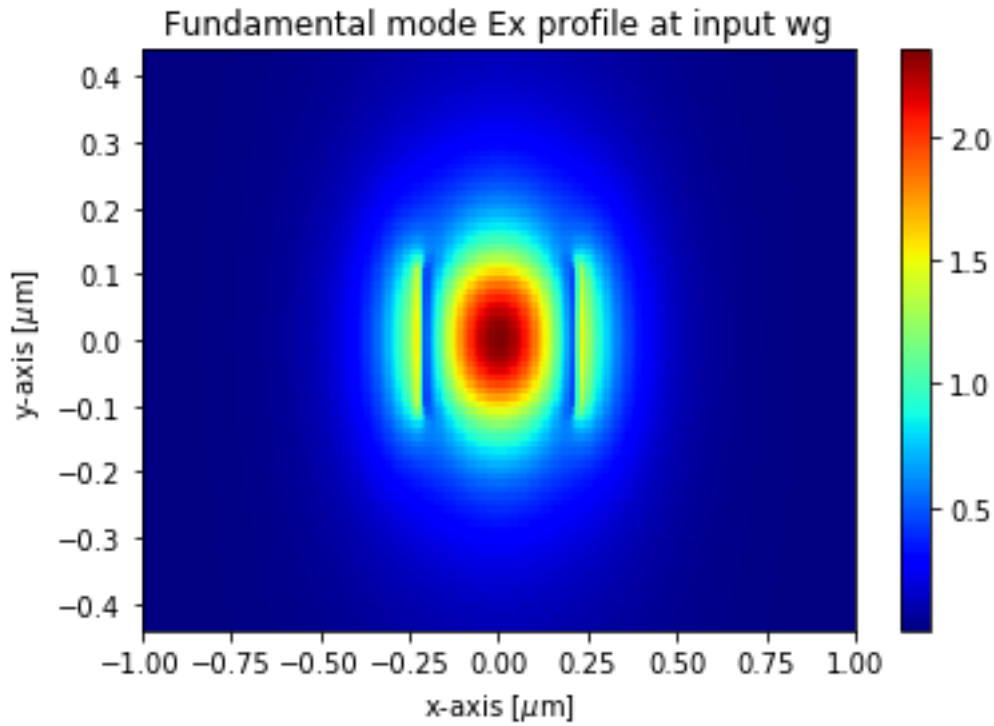
**Figure (4.20):** *Fundamental mode in typical Si waveguide with dimensions W = 0.43 μm and h = 0.22 μm*

This mode is launched at the entrance of a linear tapered interface and propagates. The output data are recorded through FDTD. We therefore obtain the data entering the FPR1 regions. Not all the fields will be represented, nevertheless it's important to plot at least the Ex component (TE component) or the power profile to understand how the fields are converted. The data out of the first interface are shown on figure 4.21.

Given that the domain on which the Ex mode on figure 4.20 and the Ex field on figure 4.21 are the same, it comes directly into sight that the profile is not the same, the 2 sides peaks disappeared and the beam in enlarged along the x-axis. This fits what was expected.
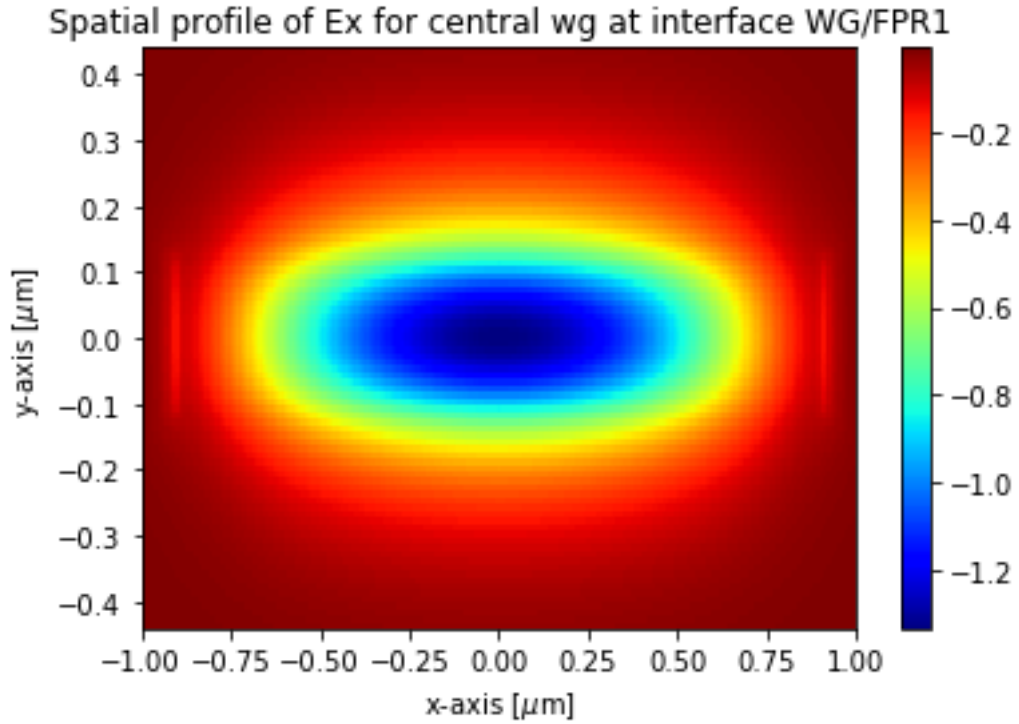
Figure (4.21): *Ex component of the field entering the FPR*

From here the Fraunhofer diffraction approximation in used to perform the Fourier transform of the input field into the FPR1. However this approximation only holds for the x-axis for which the free propagation regions approximation holds. The y-axis profile of the propagation fields, is instead, enclosed in the slab and is nothing else then a slab mode as displayed for Ex(y) on 4.15. This data is also obtained by FEM, like the input mode.
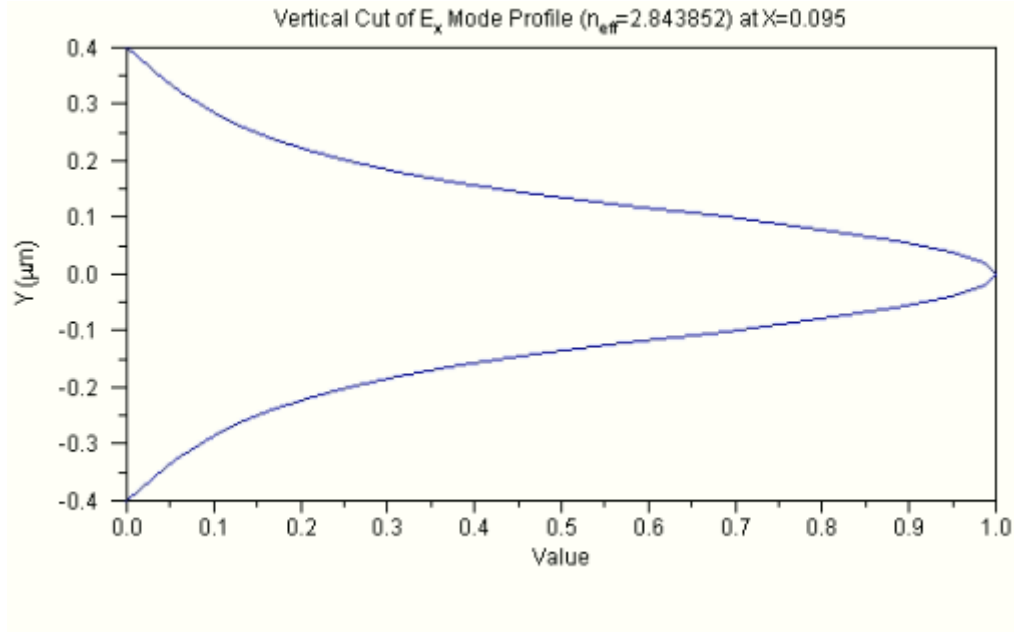
Figure (4.22): *Ex(y) profile for a simple propagating slab mode. In our device, this profile gives our Ex(y) profile at the interface FPR1/AWs.*

Finally, the far-field, broaden pattern Ex(x) is obtained as output of the Fraunhofer diffraction.
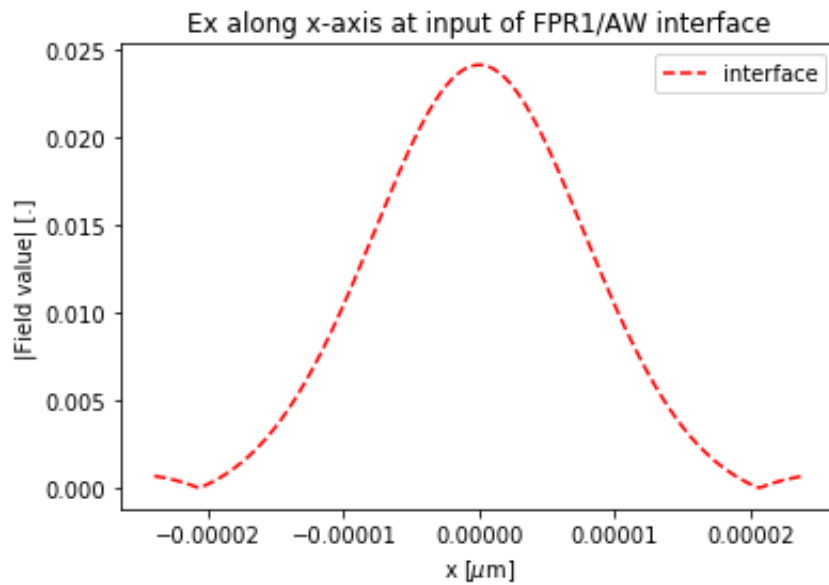
Figure (4.23): *Ex(x) at the interface FPR1/AWs with sampled value considered as constant illumination over each waveguide*

Transition regions between FPR and the AWs

At this point, the new devices come into play as it is the interface for which it is necessary to reduce the losses and for which the devices was originally designed.

The particular implementation used in this study takes advantage of the high precision of the FDTD but reduces the computation time as FDTD is only used once, for computing the transition between FPR1/AWs through one unit (the centered one) of our geometrically optimized structure.

For the input field distribution at our device we suppose :

- the Ex(x) is constant and unity over one waveguide width and therefore over our device central input waveguide width

- the Ey(y) is given by a slab mode like figure 4.22

The field in only one of the arrayed waveguides is obtained. Using this single field, we reproduce the field in each waveguide. This is performed by multiplying the field value with the factor given by the sampling of the Ex(x) profile initially striking the interface and previously obtained on figure 4.23. Those sampled values of Ex(x) are displayed on figure 4.24. The numerical method use is described as following :

$$\text{for } j = 1, \ j{+}{+}, \text{ while } k \leq N+1$$

$$\text{E\_aw[j] = E\_aw[N/2+1]*E\_sampled[j].}$$

With N+1 the total number on waveguide, E_aw[j] the field in the arrayed waveguide j, E_aw[N/2+1] is the field in the central waveguide and obtain by 3D-FDTD and finally E_sample[j] is the j-th value of the sampled profile, i.e. the green value seen figure on 4.24.
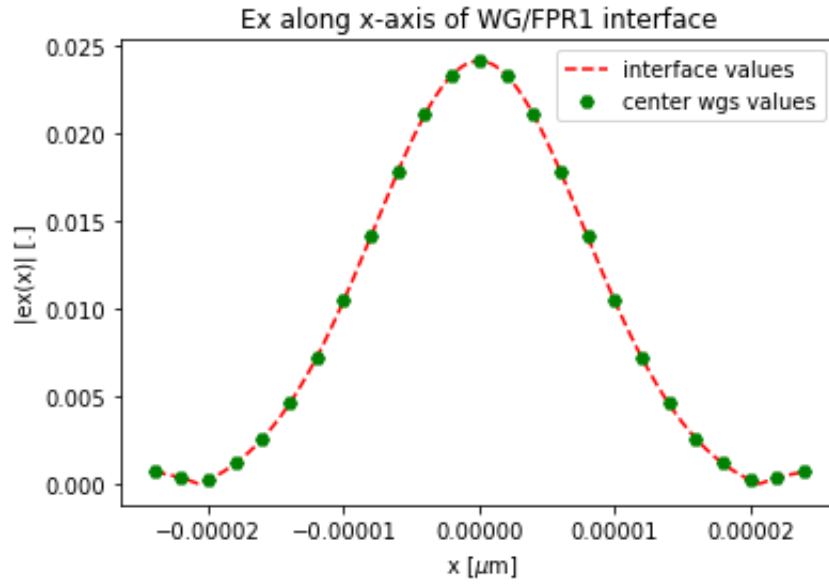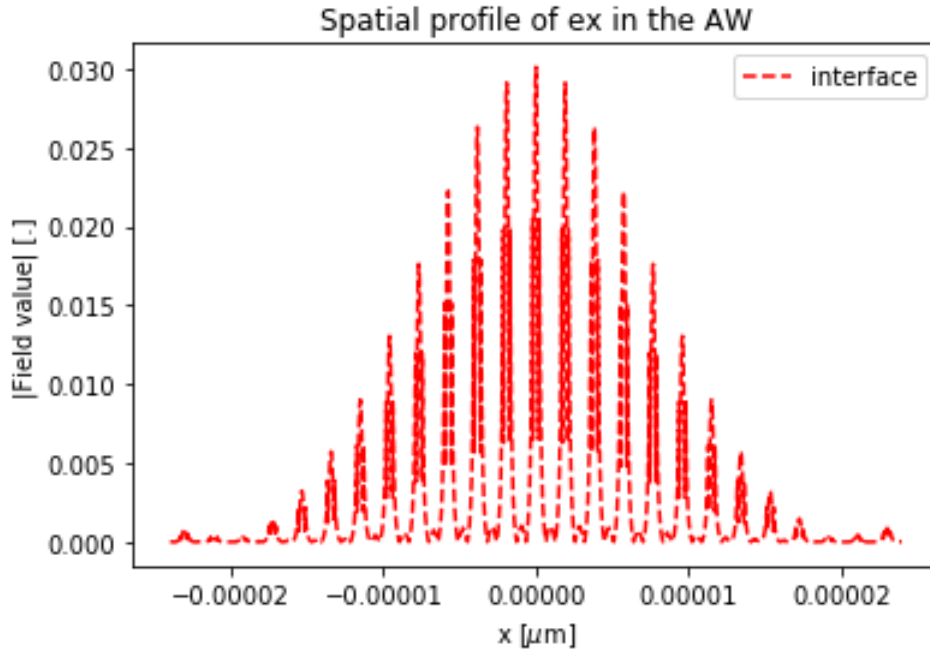
Figure (4.24): *Ex(x) at the interface FPR1/AWs the via Fraunhofer diffraction method.*

Field traveling in the AWs

At the beginning of the AWs, this is exactly the field obtained by the numerical method described right above. At the point of entering FPR2, the phase delays have acted on the signal but the amplitude profile stays the same.This is shown on figure 4.25.

Figure (4.25): *Ex(x) inside the AWs obtained from the numerical technique explained above*

Second FPR and output waveguides

The field at the input of the second FPR region can be obtained quite easily, bypassing the 2 previous steps but applying the same algorithm already described. At first, FDTD is apply twice to the same input as already described composed of :

- the Ex(x) is constant and unity over one waveguide width and therefore over our device central input waveguide width

- the Ey(y) is given by a slab mode like figure 4.22

FDTD is applied twice, the output of the first one being the input to the second.

- The first FDTD is used to simulate the FPR1/AW transition (our design)

- The second FDTD is used to simulate the AW/FPR2,low loss transition transition (linear design or our design, both are ok)

The expression has the same form has before :

E_inFPR2[j] = E_2fdtd[N/2+1]*E_sampled[j]*delta_phi[j].

Where E_inFPR2 is the input field to the second FPR, E_2fdtd is the field modified due to the two successive FDTD on the boundaries, E_sampled are the constant illuminations on each waveguide (from the sampled FPR1/AW field) and delta_phi[j] is the phase delays introduced by each array. This field is then displayed on figure 4.26
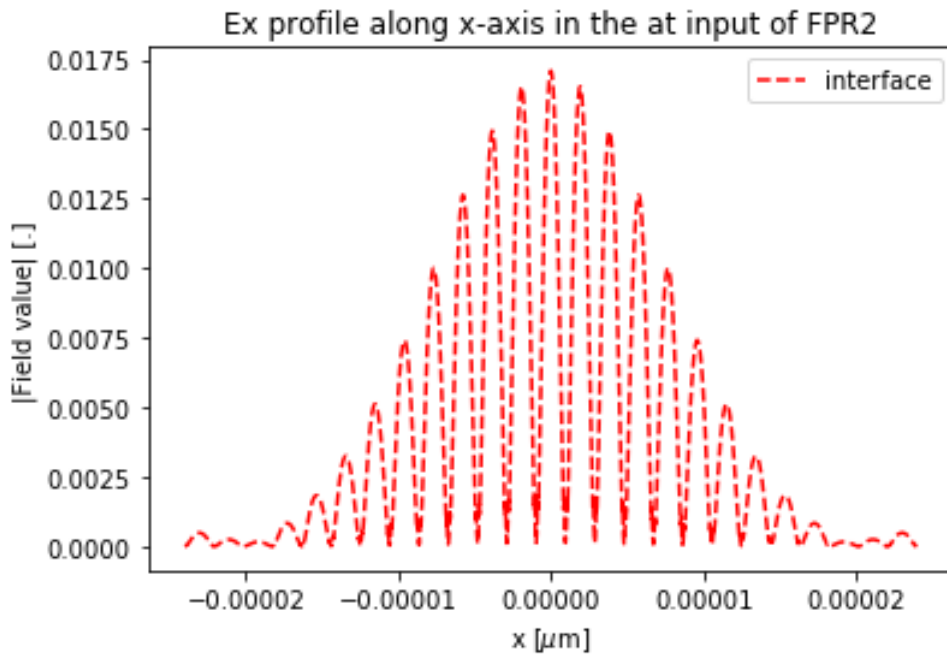
Figure (4.26): *Ex(x) at the input of the second FPR. This, using the 2 steps FDTD method*

In closing to this AWG characteristics simulation, the last step consist of applying one more time the Fraunhofer diffraction approximation. The demultiplexed wavelength profile appears at the output waveguide interface as soon as the all numerical process is repeated due to the different wavelength. The entire spectrum is not yet obtained however simulations can be carried out easily as the entire simulations in now working.

4.2.5 Commentary

The methodology behind the optimization process of the newly developed device was explained including the metrics of the normalized power but even more important the overlap integral between the field launched and the ideal field that the perfect case interface is supposed to match. After, the layout and the various parameters were presented. The geometrical optimization using data computed via 3D FDTD allowed to obtained simulated data for the metrics in the parameters space. Using and identifying the maximum values resulted in a design for which *Wmid* = 1 μm, the total length *L + Lrib* = 4.8 μm and *d* = 0.1. Etching 3D FDTD simulations were also feasible given the small dimensions of the etching areas. Including the etching in the slab with *letch* = 0.4 μm, *detch* = 0.5 μm and *wetch* = 0.2 μm, the interface loss is estimated to be 0.3 dB and account for most of the loss of light traveling through the device (the other losses are negligible) while the crosstalk is -26 dB and computed by FDTD.

However, some graphs show peculiar behavior with the overlap increasing and then decreasing with the increasing length of the taper. The reason given here was that when the tapers become longer the coupling between those increases. Finally, the AWG parameters where computed and the simulations of the characteristics were designed. Using the FDTD fields for the interfaces and customized numerical methods for the rest, the goals was to represent as best as possible the actual AWG operating characteristics. This was achieved. Step by step, the fields undergoing changes from input to the output were displayed and only the results for the centered C-band wavelength λ_0 were obtained. This simulations should be repeated for all the wavelength that constitutes the spectrum of operation. More important, the final output profile suffer some flaws which is necessary to solve. But the overall computation is really fast and easily customizable if other parameters end up being defined or in the case where parameters values need to be change.

Chapter 5

Conclusion and possible improvements

Silicon photonics has become one of the most attractive technologies for improving the transmission in optical networks as well as reducing the footprint of optical circuits. However, the high refractive index differences between different medium of a devices typically observed in transition areas leads to loss and scattering. At the same time as Silicon became popular, breakthroughs were achieved by the implementation of wavelength-division multiplexing (WDM) in networks, overcoming the shortages created by the time-division multiplexing and increasing the bit rate from 10 Gbit/s to tenth of Tbit/s. One of the main feature of the WDM is the multiplexing/demultiplexing of channels through the same fiber. This function being implemented by the arrayed-waveguide gratings. Therefore, with the boom in Si technology and WDM technology, it came naturally that the Si AWG became a major component of the optical networks. Several researches have been made for modifying some of the AWG parts to either fulfill some requirements or just to improve the characteristics performances by reducing the loss, the crosstalk between channels as well as the loss nonuniformity.

Transition regions, between the free propagation region (FPR) and the arrayed waveguides (AWs) have end up to be the most sensitive regions where most of the loss or scattering come from. Hence, special structures such as tapers or etchings are employed and allow the transition to be more adiabatic. Within this framework, this research investigated the influence of geometrically optimized taper-rib structure of several combinations. Both linear

and parabolic tapers were employed as well as combination of taper and rib "two-in-one" or taper and rib independently optimized. After the set up of the optimization methods, their constraints and the parameters involved, metrics were defined. The overlap integral between the propagating field and the fundamental mode of the Si waveguides in the waveguide array was chosen as an adequate metric. More precisely, this integral measures the coupling efficiency between the fields received at the interface and the ideal fundamental modes one desire to have in the AWs. Typically, the main goal is to reduce the loss when light transit from slab to the AWs and also avoid excitation of higher modes. In order words, it means increasing the coupling efficiency. From this point, FDTD was used to obtain the overlap and power profile and scan on the parameters. Using gradients, optimal values were found.

Consequently, linear tapers tend to be less efficient and the 2 stages structures exhibited higher power levels than the conventional or the other customized combined design. From the geometrically optimized structure, etching in the slab was introduced so as to tune the light properties at the interface by modifying the refractive index distribution. This means in order to achieve impedance matching, or more precisely, reduce the impedance mismatch between consecutive medium. Three parameters *detch*, *letch* and *wetch* were defined, scanned and optimal values found. It seems that the maximum power level of the geometrical structure alone can be surpassed. To confirm this fact, further simulations should be performed. From there, once the local optimization was finished, the AWG design parameters where computed for high-level requirement of $\lambda_0 = 1550 \mu m$, frequency channel spacing of 400 GHz and a device of $1 \times 8 channels$. It means covering almost the all C-band. Global AWG simulations of the characteristics by using intelligent and limited use of FDTD was performed with custom numerical methods. The centered wavelength properties were simulated and shown. In order to go further, this implementation enables to adapt the AWG parameters to requirement other requirements. Additionally it would be good to compute the overall wavelength output spectrum, even though this would be tedious.

Finally, a part which was not developed in the thesis, is the attempt to implement an open source automatic and gradient based optimization method for the refractive index distribution. This method would take as input the previously designed geometrical/etched optimal structure. And then, compute recursively the refractive index distribution with a gradient method based on improving the coupling efficiency (overlap integral). This would give better results and create an automatic optimization step. In conclusion, for now, estimation of the transmission values yields to a crosstalk to -25dB and the loss around 0.3 dB. A summary table of the optimized design and values is displyed on displayed on table 5.1 while the AWG design parameters and characteristics can be observed on table 5.2.

Optimal design or parameters	Value
Optimal structure	2 stage design
Optimal taper	parabolic
Optimal L	$2\ \mu m$
Optimal $Lrib$	$2.8\ \mu m$
Optimal $Wmid$	$1\ \mu m$
Optimal d	0.1
Optimal $letch$	$0.4\ \mu m$
Optimal $detch$	$0.5\ \mu m$
Optimal $wetch$	$0.2\ \mu m$

Table (5.1): *Summary table of the optimal design and values*

Design parameters	Value
Operational wavelength λ_0	1550 nm
Channel spacing Δ_{CH}	3.2 nm
Frequency channel spacing Δv	400 GHz
Number of channels N_{CH}	1×8
$\Delta\lambda$ (FSR)	25.6 nm
Free spectral range (FSR)	$1.5 \times 25.6 = 38.4$ nm
Focal length of slab waveguide (L_f)	88.803 μm
Number of arrayed waveguides (N)	25
Path difference of arrayed waveguides Δl	26.8998 μm
Separation between the input/output d_{wg}	2 μm
Gap between the waveguide gap	0.2 μm
Separation between the arrayed waveguides	2 μm
Central output loss	0.3 dB
Roughly approximated crosstalk	-25 dB

Table (5.2): *Summary of the final AWG design parameters and characteristics*

Bibliography

[1] Govind P Agrawal. *Fiber-optic communication systems*, volume 222. John Wiley Sons, 2012.

[2] Robert J Sanferrare. Terrestrial lightwave systems. *AT&T technical journal*, 66(1):95–107, 1987.

[3] D Gloge, A Albanese, CA Burrus, EL Chinnock, JA Copeland, AG Dentai, TP Lee, Tingye Li, and K Ogawa. High-speed digital lightwave communication using leds and pin photodiodes at 1.3 μm. *Bell System Technical Journal*, 59(8):1365–1382, 1980.

[4] JI Yamada, S Machida, and T Kimura. 2 gbit/s optical transmission experiments at 1.3 μm with 44 km single-mode fibre. *Electronics Letters*, 17(13):479–480, 1981.

[5] Terenuma Miya, Y Terunuma, Tatsuya Hosaka, and Tadakazu Miyashita. Ultimate low-loss single-mode fibre at 1.55 μm. *Electronics Letters*, 15(4):106–108, 1979.

[6] A Gnauck, B Kasper, R Linke, R Dawson, T Koch, T Bridges, E Burkhardt, R Yen, D Wilt, Je Campbell, et al. 4-gbit/s transmission over 103 km of optical fiber using a novel electronic multiplexer/demultiplexer. *Journal of lightwave technology*, 3(5):1032–1035, 1985.

[7] Fumihiko Kannari. Fiber links. Lecture on Optoelectronics, 2021.

[8] Katsunari Okamoto. *Fundamentals of optical waveguides*. Academic press, 2006.

[9] Thomas Welsh, Roger Smith, Haruo Azami, and Raymond Chrisner. The flag cable system. *IEEE Communications Magazine*, 34(2):30–35, 1996.

[10] Masataka Nakazawa, Masato Yoshida, and Toshihiko Hirooka. Recent progress and challenges toward ultrahigh-speed transmission beyond 10 tbit/s with optical nyquist pulses. *IEICE Electronics Express*, pages 18–20212001, 2021.

[11] Kazuro Kikuchi. Digital coherent optical communication systems: Fundamentals and future prospects. *IEICE Electronics Express*, 8(20):1642–1662, 2011.

[12] Fumihiko Kannari. Coherent optical communication technologies based on digital signal processing. Lecture on Optoelectronics, 2021.

[13] Wikipedia, internet of things. `https://en.wikipedia.org/wiki/Internet_of_things`. Accessed: 2021-12-05.

[14] Koji Yamada. Lecture notes on the evolution of silicon photonics, Novembre 2019.

[15] Cisco global cloud index, 2016-2021. `https://www.cisco.com/c/en/us/solutions/data-center-virtualization/index.html`. Accessed: 2021-07-05.

[16] Cisco vni global ip traffic forecast, 2017-2022. `https://community.cisco.com/t5/cisco-annual-internet-report/cisco-global-cloud-index-workload-data/m-p/3839818#M26`. Accessed: 2021-07-05.

[17] Koji Yamada, Tai Tsuchizawa, Hidetaka Nishi, Rai Kou, Tatsurou Hiraki, Kotaro Takeda, Hiroshi Fukuda, Yasuhiko Ishikawa, Kazumi Wada, and Tsuyoshi Yamamoto. High-performance silicon photonics technology for telecommunications applications. *Science and technology of advanced materials*, 2014.

[18] Shibnath Pathak. Photonics integrated circuits. In *Nanoelectronics*, pages 219–270. Elsevier, 2019.

[19] Michael J O'Mahony, Christina Politi, Dimitrios Klonidis, Reza Nejabati, and Dimitra Simeonidou. Future optical networks. *Journal of Lightwave Technology*, 24(12):4684–4696, 2006.

[20] Bob D Guenther and Duncan Steel. *Encyclopedia of modern optics*. Academic Press, 2018.

[21] Hiroyuki Tsuda. Lecture notes on optical networks communications, Novembre 2019.

[22] Yuki Komai, Hiroko Nagano, Kashiko Kodate, Katsunari Okamoto, and Takeshi Kamiya. Application of arrayed-waveguide grating to compact spectroscopic sensors. *Japanese journal of applied physics*, 43(8S):5795, 2004.

[23] Pradip Gatkine, Sylvain Veilleux, Yiwen Hu, Joss Bland-Hawthorn, and Mario Dagenais. Arrayed waveguide grating spectrometers for astronomical applications: new results. *Optics express*, 25(15):17918–17935, 2017.

[24] Shibnath Pathak, Michael Vanslembrouck, Pieter Dumon, Dries Van Thourhout, Peter Verheyen, Guy Lepage, Philippe Absil, and Wim Bogaerts. Effect of mask discretization on performance of silicon arrayed waveguide gratings. *IEEE Photonics Technology Letters*, 26(7):718–721, 2014.

[25] Jun Zou, Zichun Le, Jinhua Hu, and Jian-Jun He. Performance improvement for silicon-based arrayed waveguide grating router. *Optics express*, 25(9):9963–9973, 2017.

[26] WK Burns, AF Milton, and AB Lee. Optical waveguide parabolic coupling horns. *Applied Physics Letters*, 30(1):28–30, 1977.

[27] Yunfei Fu, Tong Ye, Weijie Tang, and Tao Chu. Efficient adiabatic silicon-on-insulator waveguide taper. *Photonics Research*, 2(3):A41–A44, 2014.

[28] Tong Ye, Yunfei Fu, Lei Qiao, and Tao Chu. Low-crosstalk si arrayed waveguide grating with parabolic tapers. *Optics express*, 22(26):31899–31906, 2014.

[29] Jaegyu Park, Gyungock Kim, Hyundai Park, Jiho Joo, Sanggi Kim, and Myung-Joon Kwack. Performance improvement in silicon arrayed waveguide grating by suppression of scattering near the boundary of a star coupler. *Applied optics*, 54(17):5597–5602, 2015.

[30] H Okayama, Y Onawa, D Shimura, H Takahashi, H Yaegashi, and H Sasaki. Low loss 100 ghz spacing si arrayed-waveguide grating using minimal terrace at slab–array interface. *Electronics Letters*, 52(18):1545–1546, 2016.

[31] Yusuke Sawada, Takeshi Fujisawa, Takanori Sato, and Kunimasa Saitoh. First experimental demonstration of wavefront-matching-method-designed silicon mode converters. In *2019 Optical Fiber Communications Conference and Exhibition (OFC)*, pages 1–3. IEEE, 2019.

[32] Yusuke Sawada, Takeshi Fujisawa, and Kunimasa Saitoh. Fabrication of ultrasmall silicon waveguide lenses designed by wavefront-matching method. In *2019 IEEE 16th International Conference on Group IV Photonics (GFP)*, pages 1–2. IEEE, 2019.

[33] Gang Yang, Shijie Song, Suenxin Chew, Liwei Li, and Xiaoke Yi. Inverse-design of an ultra-compact and high-efficiency silicon-on-insulator mode expander. In *2019 PhotonIcs & Electromagnetics Research Symposium-Spring (PIERS-Spring)*, pages 1493–1498. IEEE, 2019.

[34] Yusuke Sawada, Takanori Sato, Takeshi Fujisawa, and Kunimasa Saitoh. Development of the wavefront matching method based on the 3-d finite-element method and its application to si-wire mode converters. *Journal of Lightwave Technology*, 36(17):3652–3659, 2018.

[35] Andrew Michaels, Ming C Wu, and Eli Yablonovitch. Hierarchical design and optimization of silicon photonics. *IEEE Journal of Selected Topics in Quantum Electronics*, 26(2):1–12, 2019.

[36] Yohei Sakamaki, Takashi Saida, Toshikazu Hashimoto, and Hiroshi Takahashi. New optical waveguide design based on wavefront matching method. *Journal of lightwave technology*, 25(11):3511–3518, 2007.

[37] Meint K Smit and Cor Van Dam. Phasar-based wdm-devices: Principles, design and applications. *IEEE Journal of selected topics in quantum electronics*, 2(2):236–250, 1996.

[38] Pascual Munoz, Daniel Pastor, and Jose Capmany. Modeling and design of arrayed waveguide gratings. *Journal of lightwave technology*, 20(4):661, 2002.

[39] Henri Benisty. Cours d'optique physique eso1. `http://paristech.institutoptique.fr/site.php?id=7&fileid=12811`, 2015.

[40] Olivier Guilbaud. Optique appliquée. `http://hebergement.universite-paris-saclay.fr/l3papp/wp-content/uploads/2020/01/poly_optique_appliquee_2019-20.pdf`, 2019.

[41] Richard A Soref, Joachim Schmidtchen, and Klaus Petermann. Large single-mode rib waveguides in gesi-si and si-on-sio/sub 2. *IEEE Journal of Quantum Electronics*, 27(8):1971–1974, 1991.

[42] Olly Powell. Single-mode condition for silicon rib waveguides. *Journal of Lightwave Technology*, 20(10):1851, 2002.

[43] Martina de Laurentis, Andrea Irace, and Giovanni Breglio. Determination of single mode condition in dielectric rib waveguide with large cross section by finite element analysis. *Journal of Computational Electronics*, 6(1):285–287, 2007.

[44] Haowen Shu, Bitao Shen, Qingzhong Deng, Ming Jin, Xingjun Wang, and Zhiping Zhou. A design guideline for mode (de) multiplexer based on integrated tapered asymmetric directional coupler. *IEEE Photonics Journal*, 11(5):1–12, 2019.

[45] Rp photonics encyclopedia, fresnel equations. `https://www.rp-photonics.com/fresnel_equations.html`. Accessed: 2021-10-08.

[46] wikipedia, numerical analysis. `https://en.wikipedia.org/wiki/Numerical_analysis#cite_note-20c-5`. Accessed: 2021-13-05.

[47] Claude Brezinski and Luc Wuytack. *Numerical analysis: Historical developments in the 20th century*. Elsevier, 2012.

[48] *RSoft FemSIM User Guide*. Synopsys, Inc., Optical Solutions Group, 2018.12.

[49] Jean-Pierre Berenger. A perfectly matched layer for the absorption of electromagnetic waves. *Journal of computational physics*, 114(2):185–200, 1994.

[50] Dirk Schulz, Christoph Glingener, and Mark Bludszuweit. Mixed finite element beam propagation method. *Journal of lightwave technology*, 16(7):1336, 1998.

[51] Yasuhide Tsuji and Masanori Koshiba. Guided-mode and leaky-mode analysis by imaginary distance beam propagation method based on finite element scheme. *Journal of Lightwave Technology*, 18(4):618, 2000.

[52] Jian-Ming Jin. *The finite element method in electromagnetics*. John Wiley & Sons, 2015.

[53] Masanori Koshiba, Shinji Maruyama, and Koichi Hirayama. A vector finite element method with the high-order mixed-interpolation-type triangular elements for optical waveguiding problems. *Journal of lightwave technology*, 12(3):495–502, 1994.

[54] Jean-Claude Nédélec. Mixed finite elements in $\mathbf{R}^3$. *Numerische Mathematik*, 35(3):315–341, 1980.

[55] *RSoft FullWave User Guide*. Synopsys, Inc., Optical Solutions Group, 2018.12.

[56] Kunimasa Saitoh and Masanori Koshiba. Full-vectorial imaginary-distance beam propagation method based on a finite element scheme: application to photonic crystal fibers. *IEEE Journal of Quantum Electronics*, 38(7):927–933, 2002.

[57] Kane Yee. Numerical solution of initial boundary value problems involving maxwell's equations in isotropic media. *IEEE Transactions on antennas and propagation*, 14(3):302–307, 1966.

[58] Allen Taflove. The finite-difference time-domain method. 1995.

[59] Yoshiaki Tamura, Hirotaka Sakuma, Keisei Morita, Masato Suzuki, Yoshinori Yamamoto, Kensaku Shimada, Yuya Honma, Kazuyuki Sohma, Takashi Fujii, and Takemi Hasegawa. Lowest-ever 0.1419-db/km loss optical fiber. In *Optical Fiber Communication Conference*, pages Th5D–1. Optical Society of America, 2017.